Regularized Euler-α motion of an infinite array of vortex sheets

R.E.Caflisch · F.Gargano · M.Sammartino · V.Sciacca

Boll. Unione Mat. Ital. (2017) 10:113-141
DOI 10.1007/s40574-016-0097-6

Abstract We consider the Euler-α regularization of the Birkhoff-Rott equation and compare its solutions with the dynamics of the non regularized vortex-sheet. For a flow induced by an infinite array of planar vortex-sheets we analyze the complex singularities of the solutions. Through the singularity tracking method we show that the regularized solution has several complex singularities that approach the real axis. We relate their presence to the formation of two high-curvature points in the vortex sheet during the roll-up phenomenon.

Keywords Vortex-sheet · Birkhoff-Rott equation · Euler-α regularization · Complex singularities

1 Introduction

A vortex sheet is a model originally developed to approximate thin shear layers in which vorticity is highly concentrated. It is not a trivial matter to prove that the vortex sheet motion is the small thickness limit of the dynamics of shear layers; however there have been partial results where the analysis was based on formal asymptotic methods [53,28], or on numerical methods [6]. A

R.Caflisch
Mathematics Department, University of California at Los Angeles, Los Angeles, CA 90095-1555, USA E-mail: caflisch@math.ucla.edu

F. Gargano
Dipartimento di Energia, Ingegneria dell'Informazione e Modelli Matematici, University of Palermo.
E-mail: francesco.gargano@unipa.it

M. Sammartino, V. Sciacca
Department of Mathematics, University of Palermo.
E-mail: marcomarialuigi.sammartino@unipa.it
E-mail: vincenzo.sciacca@unipa.it

rigorous proof was given in [12] for the case of a layer of uniform vorticity with the interfaces having analytic regularity, see also [11]; the case of non uniform vorticity is addressed in [17]. For other cases with singular initial vorticity, see e.g. [49,50,10]

The main issue related to vortex sheets is the fact that, in their dynamics, a mechanism similar to the Kelvin-Helmholtz instability is clearly present. This instability is ultimately responsible for the ill-posedness of the Birkhoff–Rott(BR) equation. Moreover, also when considering initial conditions with analytic regularity, a class of data where the Kelvin-Helmholtz instability can be controlled, one can observe a finite-time appearance of curvature singularity. This was firstly shown by Moore in [54,55] through a remarkable analysis based on formal asymptotic expansion. Moore's results were supported by the investigation presented in [4], by direct numerical simulations [63,46,45,26, 56], and later rigorously proved in [31,20]. Local in time well-posedness of the BR equation was achieved, for analytic initial data, in [65] while, in [19], long-time existence was obtained for small perturbations of the flat profile. For a weaker notion of the solution of the BR equation see [69], where it is also shown that, under minimal regularity assumptions, the vortex-sheet is in fact analytic; see also [47].

To continue the vortex-sheet motion after the singularity requires the use of models with regularization effects such as finite sheet thickness [6], vortex blob regularization [2,5,48], Euler-α model [41,8,9], viscosity effects [67,28, 22,64,16]. Numerical results show that, before the singularity formation, these models converge to the vortex-sheet solution while allowing the continuation of the vortex-sheet solution after the blow-up.

In this paper we analyze the roll-up phenomenon arising from the regularized BR equation through the Euler-α model (hereafter BR-α). The Euler-α model was originally introduced in the Euler-Poincaré variational framework [39,40], and later used by various authors in different contexts, such as the analysis of turbulent flow, see e.g.[32], and the regularization of the vortex sheet motion in [41,8,9]. The existence of a unique global weak solution to the 2D Euler-α equation, with initial datum in the class of Radon measure, was achieved in [57]. For fixed sign measures the convergence, up to a subsequence, to a weak solution of the 2D Euler equation, was proved in [9].

As shown in [41], the BR-α model allows to continue the vortex-sheet solution after the singularity time and to follow the roll-up phenomenon in the vortex-sheet. In this paper we shall reconsider this problem from a different perspective: performing the complex singularity analysis on the solution of the BR-α equation, we shall show that, although the singularity formation is prevented, the roll-up phenomenon is related to the presence of complex singularities in the solution having similar characterization of the singularity of the non regularized BR solution. The configuration we shall take into account consists of an infinite array of vortex-sheets.

The rest of the paper is organized as follows. In Section 2 we give a short review of some of the results concerning well-posedness and singular behavior of the vortex-sheets. In Section 3 we construct the infinite array of vortex-sheets

initial datum and we perform the singularity analysis on the BR solution. In Section 4 the Euler-α model is introduced, the resulting regularized vortex-sheet motion described and the singularity analysis presented. The evolution of a thin layer of vorticity, ruled by the Euler equations, is analyzed in Section 5. Some final remark is given in Section 6.

2 Instability, ill-posedness, and short time analytic regularity

We consider the 2D Euler equation in the form

$$\partial_t \omega + \boldsymbol{u} \cdot \boldsymbol{\nabla} \omega = 0,$$

where the velocity $\boldsymbol{u}$ is expressed in terms of the vorticity as

$$\boldsymbol{u} = \mathbf{K} * \omega$$

where

$$\mathbf{K} = \frac{1}{2\pi} \frac{\boldsymbol{r}^\perp}{r^2}, \tag{2.1}$$

being $\boldsymbol{r} = (x, y)$. Notice also that the velocity can be expressed in terms of a *stream function* Ψ as

$$\boldsymbol{u} = \frac{\boldsymbol{r}^\perp}{r} D\Psi \qquad \Psi(r) \equiv \frac{1}{2\pi} \log r. \tag{2.2}$$

If one assumes that the vorticity is concentrated on a curve $y = \varphi(x, t)$ with density $\gamma(x, t)$, i.e. that

$$\omega(x, t) = \gamma(x, t)\delta(y - \varphi(x, t)),$$

one can derive, see [51], the BR equation in the form

$$\partial_t \gamma + \partial_x (U\gamma) = 0 \tag{2.3}$$
$$\partial_t \varphi + U \partial_x \varphi = V, \tag{2.4}$$

where the velocity on the curve (U, V) is given by:

$$U - iV = \int \frac{\gamma(x')}{x - x' + i\left[\varphi(x) - \varphi(x')\right]} dx' \tag{2.5}$$

2.1 Linear ill-posedness

Consider a flat vortex–sheet $\varphi = 0$ of uniform density γ_0 and consider small perturbation around this profile: $(\gamma_0 + \tilde{\gamma}, \tilde{\varphi})$. The linearization of the BR equations reads as

$$\partial_t \tilde{\gamma} = -\gamma_0 \partial_x \tilde{U}$$
$$\partial_t \tilde{\varphi} = \tilde{V}$$

where

$$\tilde{U} = -\gamma_0 \left[\text{sign}(x) \frac{1}{2\pi|x|} \right] * \partial_x \tilde{\varphi}$$
$$\tilde{V} = \left[\text{sign}(x) \frac{1}{2\pi|x|} \right] * \tilde{\gamma}$$

If one writes the above system in the Fourier space one gets

$$\partial_t \tilde{\gamma}(\xi) = i \frac{\gamma_0^2}{2} \xi^2 \text{sign}(\xi) \tilde{\varphi}(\xi)$$
$$\partial_t \tilde{\varphi}(\xi) = -i \frac{1}{2} \text{sign}(\xi) \tilde{\gamma}(\xi)$$

which gives

$$\tilde{\gamma}(\xi), \tilde{\varphi}(\xi) \sim \exp\left(|\gamma_0||\xi| t/2\right) \tag{2.6}$$

The above exponential amplification law for the spectrum (the higher the Fourier mode, the larger the exponential amplification) is equivalent to the linear ill–posedness of the BR equation.

The same analysis can be carried if one uses the lagrangian formulation of the BR equation. Following Saffman [62] we write:

$$\partial_t \bar{Z}(\Gamma, t) = -\frac{i}{2\pi} \int \frac{d\Gamma'}{Z(\Gamma, t) - Z(\Gamma', t)} \tag{2.7}$$

In this formulation the flat uniform sheet is expressed by $Z = \Gamma/\gamma_0$, and we write a small periodic perturbation of this profile as

$$Z = \frac{\Gamma}{\gamma_0} + \sum_{n=-\infty}^{\infty} a_n(t) e^{in\Gamma\alpha}$$

where the parameter α is related to the wavelength of the perturbation: in particular, for $\gamma_0 > 0$, the wavelength λ, as measured in the physical space, is $\lambda = 2\pi/(\alpha\gamma_0)$; thereofore a 2π periodic perturbation corresponds to $\alpha = 1/\gamma_0$. Substituting the above expression in the BR equation, to first order in the size of the perturbation, one derives the following equations for the coefficients a_n

$$\partial_t \bar{a}_n = -i \frac{n\alpha\gamma_0^2}{2} a_{-n} \tag{2.8}$$

that give a_n to grow like $e^{\sigma t}$ with $\sigma = n\alpha\gamma_0^2/2$. This result, for 2π-periodic perturbations, is consistent with (2.6). This kind of exponential growth of small perturbation leads to linear ill–posedness of the BR equation. In fact, see [13], one can construct a solution of the linearized BR equation in the form

$$y = \varepsilon \sum A_n \sin \frac{n\pi x}{\lambda} \exp \frac{n\pi\gamma_0 t}{\lambda}$$

and choosing $A_n = \exp\left(-|n|^{1/2} - n\pi\gamma_0 t_0/\lambda\right)$ one gets a solution that is C^∞ for $t < t_0$ but with infinite norm in any Sobolev space for $t > t_0$.

2.2 Well posedness results

If the initial data are analytic one can prove that the BR equation are well posed. In what follows we shall denote by $D(\rho)$ the strip of the complex plane of width $\rho > 0$:

$$D(\rho) \equiv \{(x,\eta) :\ x \in \mathbb{R}/\pi\mathbb{Z}\,, |\eta| < \rho\}\ ,$$

For a function $f : D(\rho) \to \mathbb{C}$ we introduce the notation:

$$|f|_\rho \equiv \sup_{(x,\eta)\in D(\rho)} |f(x+i\eta)|\ ,$$

$$|f|_\rho^{(\alpha)} \equiv \sup_{(x,\eta),\,(\bar{x},\eta)\in D(\rho)} \frac{|f(x+i\eta) - f(\bar{x}+i\eta)|}{|x-\bar{x}|^\alpha}$$

Definition 2.1 Let $f : D(\rho) \to \mathbb{C}$ analytic. Then se say $f \in B_\rho$ when:

$$\|f\|_\rho \equiv |f|_\rho + |f|_\rho^{(\alpha)} < \infty$$

Definition 2.2 Let $f : D(\rho) \to \mathbb{C}$ analytic. then we say $f \in B_\rho^m$ when:

$$\|f\|_{m,\rho} \equiv \sum_{j\le m} |\partial_x^j f|_\rho + |\partial_x^m f|_\rho^{(\alpha)} < \infty$$

Definition 2.3 Let $t \in [0,T]$ and let β and ρ be such that $\beta T < \rho$. A function $f(\cdot,\cdot)$ will be said to be in $B^m_{\rho,\beta,T}$ when $f(\cdot,t) \in B^m_{\rho-\beta t}$ $\forall t \in [0,T]$ and when:

$$\|f\|_{m,\rho,\beta,T} \equiv \sum_{j\le m} \sup_{0\le t\le T} |\partial_x^j f(\cdot,t)|_{\rho-\beta t} + \sup_{0\le t\le T} |\partial_x^m f(\cdot,t)|^{(\alpha)}_{\rho-\beta t} < \infty$$

One can prove the following result [65].

Theorem 2.1 (Sulem,Sulem,Bardos and Frisch, 1981) *Suppose the initial data $\varphi_0 \in B^2_{\rho_0}$ and $\gamma_0 \in B^1_{\rho_0}$. Then there exists $\beta > 0$ such that Eqs. (2.3)-(2.4) admit a unique solution (γ,φ) with $\gamma \in B^1_{\rho_0,\beta,T}$, $\varphi \in B^2_{\rho_0,\beta,T}$.*

The proof is based on the following estimate which bounds the velocity (U,V) in terms of the jump strength γ and of the norm of the base curve φ.

Proposition 2.1 *Let $(\gamma,\varphi) \in B^1_{\rho_0} \times B^2_{\rho_0}$. Then the velocity (U,V), as expressed by (2.5) is in $B^1_{\rho_0} \times B^1_{\rho_0}$, and the following estimate holds:*

$$\|(U,V)\|_{1,\rho} \le c\,(\|\gamma\|_{1,\rho} + \|\varphi\|_{2,\rho})$$

2.3 Finite time singularity and ill–posedness of the BR equation

The linear ill–posedness, in general, does not necessarily mean that the equation is ill-posed, as non linearities, when the initial small disturbance grows in size, cannot be neglected and could tame the exponential growth of higher Fourier modes. In [54] Moore gave a formal asymptotic analysis of the nonlinear effects. He constructed a solution that develops, in finite time, a singularity; the intensity of the vorticity remains finite but behaves, at the singularity time as $|x|^{1/2}$ so that a blow up in the derivative is present. At the singularity time the shape of the curve forms a cusp: the tangent to the curve, behaves, as $|x|^{3/2}$, so that a blow up of the curvature of the sheet is present.

A rigorous proof of the finite–time singularity formation and of ill–posedness was achieved by Caflisch and Orellana in [20]. They where able to construct a solution of BR equation (2.7) in the form:

$$Z(\Gamma, t) = \Gamma + S_0 + r. \tag{2.9}$$

The term S_0 solves the linearized BR equation, where linearization is performed close to the flat sheet with intensity $\gamma_0 = 1$, and develops a finite time singularity. It is interesting to notice that equation (2.8) shows that the linearized BR evolution can be written in terms of the Hilbert transform H

$$\partial_t \bar{Z} = \frac{\gamma_0}{2} H[\partial_\Gamma Z], \tag{2.10}$$

where we are considering 2π-periodic odd disturbances, and the Hilbert transform is defined, in terms of its symbol, as $H = \mathrm{sign}(n)$.

The term r corrects for nonlinear effects and, in [20], it is shown to be small, so that the singular behavior is preserved by the nonlinear evolution. An example of the singular solution is:

$$S_0(\Gamma, t) = \varepsilon(1-i)\left[\left(1 - e^{-t/2 - i\Gamma}\right)^{1+\nu} - \left(1 - e^{-t/2 + i\Gamma}\right)^{1+\nu}\right]$$

where $\varepsilon > 0$ is small and ν is chosen such that $0 < \nu < 1$. One immediately recognizes that, at time $t = 0$, S_0 develops the kind of singularity predicted by the formal analysis of Moore. More precisely one can say:

1. S_0 solves the linear equation (2.10)
2. S_0 is analytic in the strip $|\mathrm{Im}\Gamma| < t/2$ for $t > 0$
3. S_0 is small and decays as $t \to \infty$. At $t = 0$ S_0 has a singularity in its $(1+\nu)$-th derivative.

The result proven by Caflisch and Orellana is the following.

Theorem 2.2 (Caflisch and Orellana, 1989) *Suppose that S_0 satisfies 1.-3. above. Then there exists $r(\Gamma, t)$ such that* (2.9) *is a solution of the BR equation and*

$$\|r\|_{1,0} < c\varepsilon^2 e^{-|t|/2}.$$

Moreover $\partial_{\Gamma\Gamma} r = O(\varepsilon^2)$ and has the same blow up as S_0.

The above finite time singularity construction, together with the fact that solution of the BR equation are preserved by the following transformations

$$Z_b(\Gamma,t) = Z(\bar{\Gamma},-t) \qquad Z_s(\Gamma,t) = Z(\Gamma,t-t_0) \qquad Z_n(\Gamma,t) = n^{-1}Z(n\Gamma,nt)$$

where used in [20] to construct solutions that blow–up in an arbitrarily short time.

Theorem 2.3 (Ill-posedness of the BR equation, Caflisch and Orellana 1989) *For any positive $\nu, k, \varepsilon, \delta$ there is an initial datum $Z = \Gamma + S_0$ such that $|S_0|_{H^k} < \varepsilon$ and such that $\sup|\partial_\Gamma^{1+\nu} Z|$ goes to infinity for $t = t_0 < \delta$.*

3 Infinite array of periodic vortex sheets

In this section we present a numerical study of the singularity formation for a vortex sheet curve. The initial configuration consists on a infinite array of planar inviscid vortex sheet curves, periodic in the tangential direction and evenly distributed along the normal variable. The geometry of the problem is illustrated in Fig.1: across each curve the velocity field experiences a jump in the component tangential to the curve, passing from $\mathbf{v}_-$ to $\mathbf{v}_+$. The vorticity is concentrated along the curves and is zero outside and can therefore be expressed as

$$\omega(x(p,t),y(p,t)) = \sum_{h\in\mathbb{Z}} \hat{\gamma}\delta(\mathbf{x}_h(p,t)),$$

where $\mathbf{x_h}(p,t) = (x(p,t), y(p,t) - hL_y)$ is a parametrization of the h-th vortex sheet curve, p is a Lagrangian variable chosen to be constant along paths moving with the average of the velocities on either side of the sheet, and δ is the Dirac function. The jump in the velocity across a sheet is given by the true vortex sheet strength $\hat{\gamma} = (\mathbf{v}_+ - \mathbf{v}_-) \times \boldsymbol{n}$, being $\boldsymbol{n}$ the normal vector pointing in planar region where the velocity field is given by $\mathbf{v}_+$. The circulation Γ along particle paths is conserved. In particular, indicating with $s(p)$ the arc length in p, the circulation $d\Gamma$ along the path $(s(p), s(p+dp))$ is conserved, and from $\hat{\gamma} = d\Gamma/ds$ follows that $\gamma(p) = \hat{\gamma}(p,t)|\partial_p \mathbf{x}_h(p,t)|$ does not depend on time.

Assuming that each vortex-sheet curve is L_x periodic in the x-direction, and that L_y is the distance between two consecutive curves along the y-direction, see Fig.1, the periodicity conditions of the problem are

$$x(p+kL_x,t) = kL_x + x(p,t), y(p+kL_x,t) = y(p,t), \gamma(p+kL_x) = \gamma(p),$$

for $k \in \mathbb{Z}$, and γ is equal for all the sheets. The motion of the generic marker $\mathbf{x}(p,t)$ of a sheet (hereafter we shall omit the subscript h in $\mathbf{x}_h$) is governed by the BR equation that, in terms of the parametrization p of the curve, is written as:

$$\frac{\partial \mathbf{x}(p,t)}{\partial t} = \int_{-L_x/2}^{L_x/2} \gamma(\tilde{p})\mathbf{K}_{L_x,L_y}(\mathbf{x}(p,t) - \mathbf{x}(\tilde{p},t)))d\tilde{p}. \tag{3.11}$$

In (3.11) the kernel $\mathbf{K}_{L_x,L_y}$ has to take into account the periodicity of the problem, and it can be obtained from

$$\mathbf{K}_{L_x,L_y}(\mathbf{x}) = \left(\frac{\partial \Psi_{L_x,L_y}}{\partial y}(x,y), -\frac{\partial \Psi_{L_x,L_y}}{\partial x}(x,y) \right), \tag{3.12}$$

where Ψ_{L_x,L_y} is the streamfunction solution of the following 2D periodic problem in the domain $\Omega = [-L_x/2, L_x/2] \times [-L_y/2, L_y/2]$:

$$\begin{cases} \nabla^2 \Psi_{L_x,L_y}(x,y) &= -\delta(x,y), \\ \Psi_{L_x,L_y}(-L_x/2, y) = \Psi_{L_x,L_y}(L_x/2, y), & \forall y \in [-L_y/2, L_y/2] \\ \Psi_{L_x,L_y}(x, -L_y/2) = \Psi_{L_x,L_y}(x, L_y/2), & \forall x \in [-L_x/2, L_x/2] \end{cases} \tag{3.13}$$

The solution of (3.13), up to a constant, is reported in [1]

$$\Psi_{L_x,L_y}(x,y) = \frac{x^2}{2L_xL_y} - \frac{1}{2\pi} \log \left| \theta_1 \left(\pi(i\frac{x}{L_y} + \frac{y}{L_y}), e^{-\pi \frac{L_x}{L_y}} \right) \right|, \tag{3.14}$$

where we have introduced the Jacobi theta function of the first kind $\theta_1(z,q) = 2\sum_{n=0}^{\infty}(-1)^n q^{(n+1/2)^2} \sin[(2n+1)z]$. Hence the kernel $\mathbf{K}_{L_x,L_y}$ has the following components:

$$\begin{aligned} \mathbf{K}_{L_x,L_y}(\mathbf{x}) = \Bigg(& -\frac{1}{2L_y} \Re \left[\frac{\theta_1' \left(\pi(i\frac{x}{L_y} + \frac{y}{L_y}), e^{-\pi \frac{L_x}{L_y}} \right)}{\theta_1 \left(\pi(i\frac{x}{L_y} + \frac{y}{L_y}), e^{-\pi \frac{L_x}{L_y}} \right)} \right], \\ & -\frac{x}{L_xL_y} - \frac{1}{2L_y} \Im \left[\frac{\theta_1' \left(\pi(i\frac{x}{L_y} + \frac{y}{L_y}), e^{-\pi \frac{L_x}{L_y}} \right)}{\theta_1 \left(\pi(i\frac{x}{L_y} + \frac{y}{L_y}), e^{-\pi \frac{L_x}{L_y}} \right)} \right] \Bigg). \end{aligned} \tag{3.15}$$

Notice that $\mathbf{K}_{L_x,L_y}$ is singular in $(0,0)$ and therefore the integral in (3.11) is intended in a principal value sense. To analyze the singularity formation process of the BR equation we need to give an accurate evaluation of the right hand side of (3.11). This is accomplished by using standard numerical procedures for vortex sheet computations. In particular we use a fourth order Runge–Kutta scheme as temporal discretization, and integration in (3.11) is performed by using the alternating point quadrature formula, see [46]. Regarding the evaluation of the θ_1 function it is enough to only consider the first 20 terms of the summation, as the various terms rapidly decrease with n. To avoid that Kelvin-Helmholtz instability leads to the growth of the round-off disturbances we apply the Fourier filtering technique proposed by Krasny in [46]: at each time step the Fourier modes of the solution having amplitude less than the threshold value 10^{-27} are set to zero. Computation is performed with 32-digit precision.

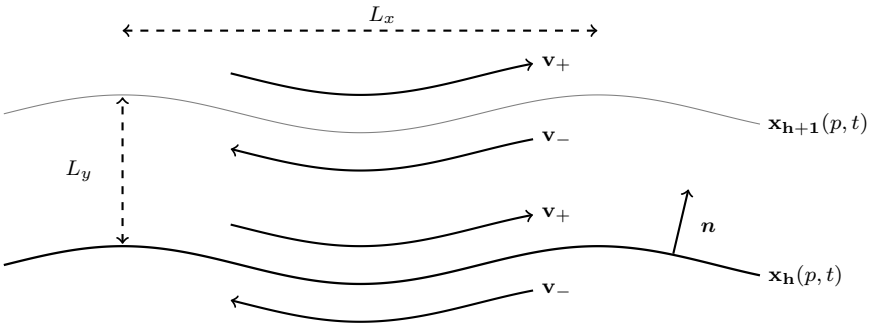

Fig. 1 Scheme of the infinite array of periodic vortex sheet curves. Each curve $\mathbf{x_h}(p,t)$ represents a vortex sheet curve, periodic in the $x-$direction.

3.1 Singularity formation for Birkhoff-Rott equation

In this section we give a numerical construction of the finite–time singularity of the BR equation (3.11). As initial condition we consider the sinusoidal perturbation of a flat sheet

$$\mathbf{x}(p,0) = (p, 0.5\sin(p)), \quad \gamma(p) = 1, \quad p \in [-\pi, \pi], \tag{3.16}$$

and $L_x = L_y = 2\pi$.

To follow the process of the singularity formation we apply the *singularity tracking method*. If a solution develops a real singularity the method, before the blow-up, allows to determine the position and the character of the complex singularity that is the nearest to the real axis. This technique has been widely used to capture the singular behavior of several solutions of equations arising in fluid dynamics. Besides the cited papers regarding the vortex-sheet singularity formation, singularity tracking has been applied to investigate the complex singularities of the incompressible Euler flow, [66,14,33,59,52,23], to follow the singularity formation for Prandtl solution in [25,27,35] and to investigate on the connection with the separation phenomena in the zero viscosity limit [36–38]. In this context also equations with dispersive character have been recently analyzed: we mention the Camassa-Holm and Degasperi-Procesi equations in [27,24], the nonlinear Schrödinger equation in [61], the KdV equation in [42, 34], and others [42–44]. See also the recent review paper [15] on the various singularity tracking procedures.

Here we apply the singularity tracking to the Fourier modes of the components

$$(X(p,t), Y(p,t)) = (x(p,t) - p, y(p,t)) = \left(\sum_k X_k(t) e^{ikp}, \sum_k Y_k(t) e^{ikp} \right),$$

obtained from the numerical solution of (3.11). The method is based on the assumption, see [21], that if $X(p,t)$ has a complex singularity in $z_s(t) = \xi_X(t) +$

$i\delta_X(t)$ of order $\mu_X(t) + i\tau_X(t)$, then the Fourier modes of X have the following asymptotic behavior:

$$X_k(t) \approx C_X(t) k^{-(\mu_X(t)+1)} e^{-\delta_X(t)k} \sin(k\xi_X(t) + \tau_X(t)\log(k) + \phi_X(t)). \quad (3.17)$$

In principle the parameters $C_X, \mu_X, \delta_X, \xi_X\tau_X, \phi_X$ in (3.17) should be at each time independent of the value of k although in practice the parameters are better estimated in specific band of k. Hence, as previously done by other authors, see for instance [3], we suppose that (3.17) holds point-wise for each k, and equating six consecutive modes $X_{k-5}, X_{k-4}, X_{k-3}, X_{k-2}, X_{k-1}, X_k$ to the form in (3.17) we obtain a nonlinear system for the parameters $C_X, \mu_X, \delta_X, \xi_X\tau_X, \phi_X$ whose solution returns the k-dependent values of the parameters. We have found at each time that $C_X, \mu_X, \delta_X, \xi_X\tau_X, \phi_X$ are actually k-independent in the range of the first $30 - 50$ wavenumbers (see Fig.2), hence at each time we assume as values for the various parameters in (3.17) those obtained in this range of wavenumbers. Both components have a singularity in the same position in the complex plane (that is $\delta_X(t) \approx \delta_Y(t)$ and $\xi_X(t) \approx \xi_Y(t)$), while the two characterizations μ_X and μ_Y are slightly different. The time evolution of $\delta_X(t)$ and $\xi_X(t)$ is shown in Figs.3a-b: at $t_c \approx 1.507$ $\delta_X(t_c) \approx 0$ and $\xi_X(t_c) \approx 1.288$. The time evolution of $\mu_X(t), \mu_Y(t)$ is shown in Fig.3c: at the singularity time $t_s = 1.507$ we have obtained $\mu_X(t) \approx 1.61$, $\mu_Y(t) \approx 1.725$, meaning that both the components $(X(p,t), Y(p,t))$ experience at t_s a blow-up in their second derivative in $p^* \approx 1.288$. Regarding the values of τ_X, τ_Y we have obtained that they are of order 10^{-1} at t_s. As X and Y have a blow up in their second derivatives, the curve at time t_s remains smooth as shown in Fig.4a. Also the curvature $\kappa(p,t) = (x_p y_{pp} - y_p x_{pp})/((x_p^2 + y_p^2)^{3/2})$ and the true vortex sheet strength $\hat{\gamma}(p,t) = \gamma(p)/|(x_p, y_p)|$ become singular at t_s. Applying the singularity tracking method to κ and $\hat{\gamma}$ as function of p, we obtain that κ forms a singularity in p^* having characterization $\mu_\kappa \approx -0.46$, while $\hat{\gamma}$ forms a singularity in p^* having characterization $\mu_{\hat{\gamma}} \approx 0.54$[1]. This means that the curvature κ diverges close p^*, in particular κ diverges positively at p^{*-} and negatively at p^{*+}, while the true vortex sheet strength $\hat{\gamma}$ has a square-root cusp behavior at p^*. The curvature κ and the true vortex sheet strength $\hat{\gamma}$ are shown in Figs.4b-c at $t = 1.505$ as functions of the signed archlenght from $p = 0$ (only positive arc length are shown): the divergent behavior of κ and the cusp behavior of $\hat{\gamma}$ can be seen close $s(p^*) \approx 1.166$.

All the characterizations of the singularities of X, Y, κ and $\hat{\gamma}$ are in full agreement with those predicted by Moore in his analysis on the vortex-sheet curvature singularity formation [54], where the predicted values are $3/2$ for X, Y, $-1/2$ for κ and $1/2$ for $\hat{\gamma}$.

[1] In both cases the imaginary part of the complex characterizations due to the asymptotic behavior in (3.17) is negligible.

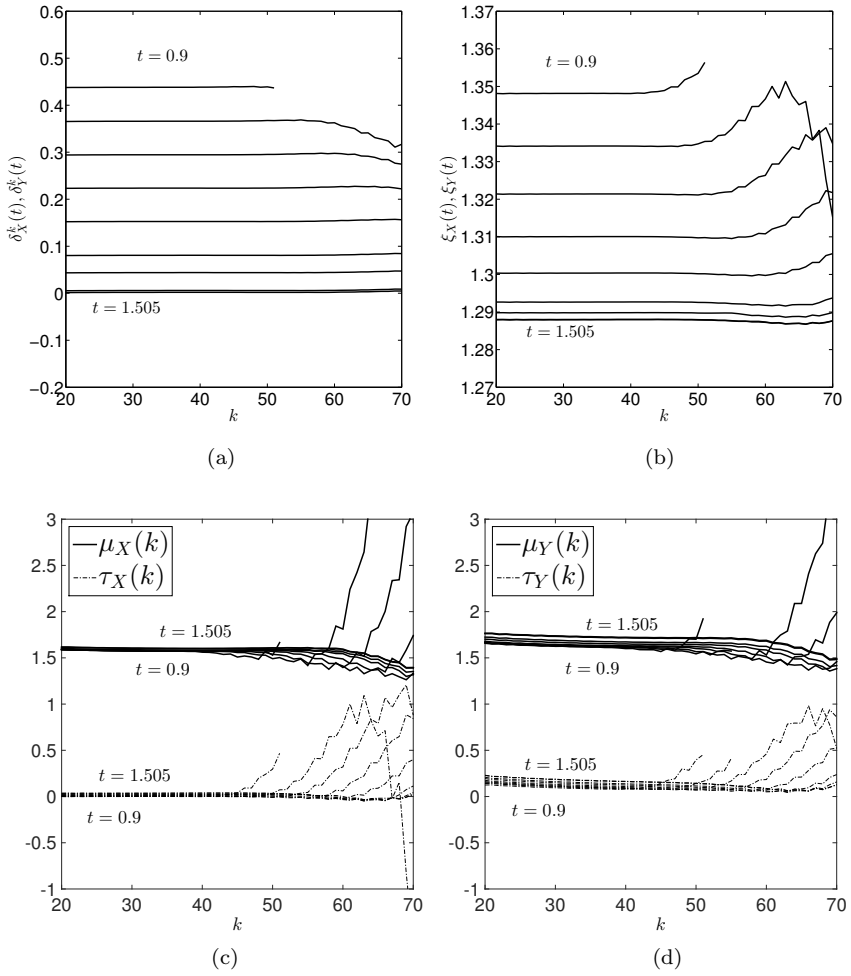

Fig. 2 Results of the numerical fitting of (3.17) from $t = 0.9$ up to $t = 1.5$,increments of 0.1, and $t = 1.505$. **(a)** Fitting of the width of analyticity strip δ_X, δ_Y of the components of the curve X, Y. For all time $\delta_X \approx \delta_Y$. δ_X is k-independent in a range of wavenumber k whose size increases in time. **(b)** Fitting of the positions of the real part $\xi_X, \xi_Y$of the singularities of X, Y. For all time $\xi_X \approx \xi_Y$. ξ_X is k-independent in the range of the first 50 wavenumber. **(c)** Fitting of the real part μ_X and of the imaginary part τ_X of the characterization of the singularity of X. At $t = 1.505$ The k-independent value of μ_X is 1.62, while $\tau_X \approx 10^{-3}$. **(d)** Fitting of the real part μ_Y and of the imaginary part τ_Y of the characterization of the singularity of Y. At $t = 1.505$ the k-independent value of μ_Y is 1.72, while $\tau_Y \approx 10^{-1}$.

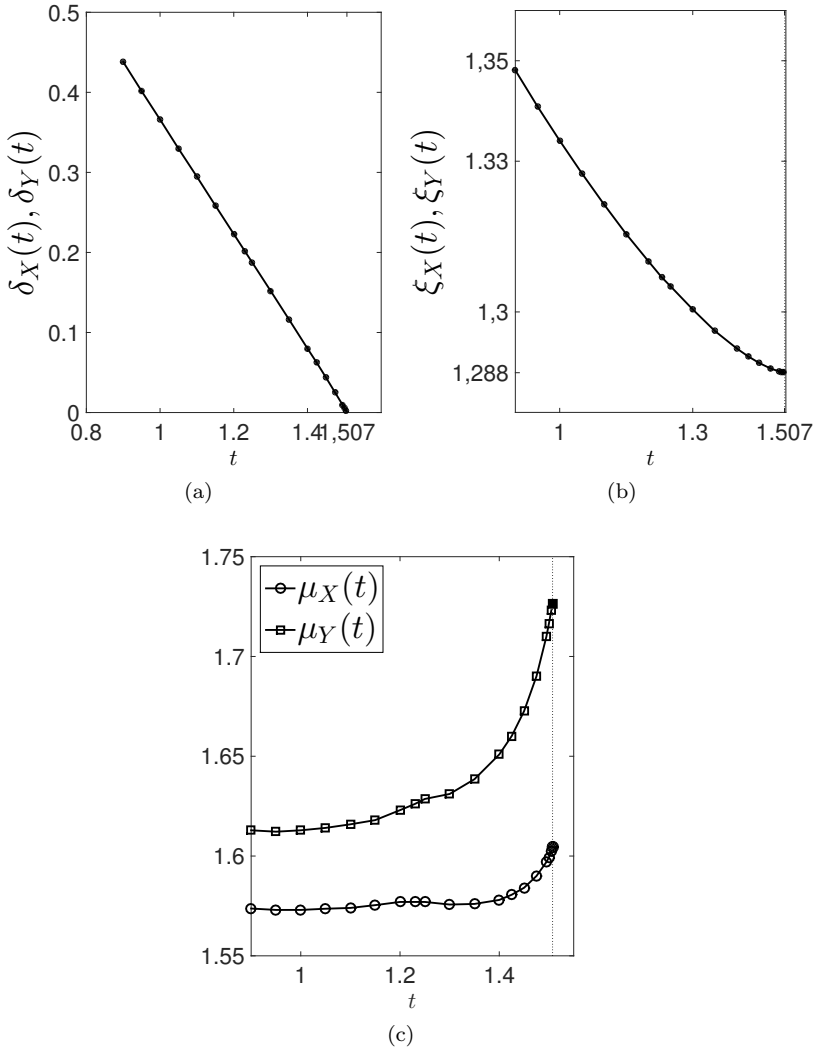

Fig. 3 a) The distances $\delta_X = \delta_Y$ from the real plane of the singularity of the BR solution. **b)** Real part of the complex position of the singularity of the BR solution. **c)** Time evolution of the characterizations μ_X, μ_Y of the singularities. Tracking is from $t = 0.9$ to $t = 1.505$, time steps of 0.05. At $t \approx 1.507$ both components of the BR solution become singular due to singularities of characterizations $\mu_X \approx 1.72, \mu_Y \approx 1.62$.

4 Regularization of the Birkhoff-Rott equation: the BR-α model.

The α-regularization arises when one derives the velocity from the vorticity through a regularized kernel; i.e.

$$\boldsymbol{u} = \mathbf{K}^{\alpha} * \omega, \tag{4.18}$$

where

$$\mathbf{K}^\alpha = G_\alpha * \mathbf{K} \qquad \text{with} \quad G_\alpha \equiv \frac{1}{\alpha^2}\frac{1}{2\pi}K_0\left(\frac{r}{\alpha}\right) \tag{4.19}$$

being K_0 the modified Bessel function of the second kind of order 0. The function G^α is the Green function associated with the Helmholtz operator $L_\alpha^{-1} = \left(\mathbb{I} - \alpha^2\Delta\right)$. As for the Euler equation, and analogously to (2.2), one can write the velocity in terms of a stream function Ψ^α

$$\boldsymbol{u} = \frac{\boldsymbol{r}^\perp}{r} D\Psi^\alpha \qquad \Psi^\alpha(r) \equiv \frac{1}{2\pi}\left[\log r + K_0\left(\frac{r}{\alpha}\right)\right].$$

When the flow is governed by the Euler-α equation, and assuming the configuration of the vortex-sheet type, one can derive [9] the BR-α equation:

$$\partial_t Z(\Gamma, t) = \int \mathbf{K}^\alpha \left(Z(\Gamma, t) - Z(\Gamma', t)\right) d\Gamma'$$

In [8,9] it is proved the global well posedness of the BR-α equation. Define:

$$|Z|_* = \inf \frac{|Z(\Gamma) - Z(\Gamma')|}{|\Gamma - \Gamma'|}$$

Theorem 4.4 (Bardos,Linshiz and Titi, 2008) *Suppose $Z_0(\Gamma)$ belongs to $C^{1,\beta}$ with $0 < \beta < 1$, and that $|Z_0|_* > 0$. Then, for any $T > 0$, there exists a unique solution of the Euler-α equation with initial datum $Z(\Gamma, 0) = Z_0$.*

4.1 Euler-α regularization for the infinite array of vortex sheets

Following the framework introduced in the previous Section, the regularized kernel $\mathbf{K}^\alpha_{L_x,L_y}$ is defined by applying L_α, the inverse of Helmholtz operator, to the singular kernel $\mathbf{K}_{L_x,L_y}$ that we defined in Section 3:

$$\mathbf{K}^\alpha_{L_x,L_y} = L_\alpha(\mathbf{K}_{L_x,L_y}) = G_\alpha * \mathbf{K}_{L_x,L_y} \quad \text{in} \quad \Omega, \tag{4.20}$$

The definition of $\mathbf{K}^\alpha_{L_x,L_y}$ is equivalent to define the regularized streamfunction $\Psi^\alpha_{L_x,L_y}$ such that

$$\mathbf{K}^\alpha_{L_x,L_y}(\mathbf{x}) = \left(\frac{\partial\Psi^\alpha_{L_x,L_y}}{\partial y}(x,y), -\frac{\partial\Psi^\alpha_{L_x,L_y}}{\partial x}(x,y)\right). \tag{4.21}$$

It follows from (4.21) that $\Psi^\alpha_{L_x,L_y}$ satisfies in Ω

$$\begin{aligned}\Delta\Psi^\alpha_{L_x,L_y}(x,y) = -\nabla\times\left(L_\alpha(\mathbf{K}_{L_x,L_y})\right) = -\nabla\times(G_\alpha * \mathbf{K}_{L_x,L_y}) = \\ -G_\alpha * (\nabla\times\mathbf{K}_{L_x,L_y}) = -G_\alpha * \delta(x,y) = -L_\alpha(\delta(x,y)).\end{aligned} \tag{4.22}$$

Hence $\Psi^\alpha_{L_x,L_y}$ solves the following 2D periodic problem in Ω:

$$\begin{cases} (\Delta - \alpha^2\Delta^2)\Psi^\alpha_{L_x,L_y}(x,y) = -\delta(x,y), \\ \Psi^\alpha_{L_x,L_y}(-L_x/2, y) = \Psi^\alpha_{L_x,L_y}(L_x/2, y), \quad \forall y \in [-L_y/2, L_y/2], \\ \Psi^\alpha_{L_x,L_y}(x, -L_y/2) = \Psi^\alpha_{L_x,L_y}(x, L_y/2), \quad \forall x \in [-L_x/2, L_x/2]. \end{cases} \tag{4.23}$$

It easy to check that the solution of (4.23) is

$$\Psi^{\alpha}_{L_x,L_y} = \Psi_{L_x,L_y} + \alpha^2 G_\alpha, \tag{4.24}$$

and G_α is the solution of

$$\begin{cases} (\mathbb{I} - \alpha^2 \Delta) G_\alpha(x,y) = -\delta(x,y), \\ G_\alpha(-L_x/2, y) = G_\alpha(L_x/2, y), \quad \forall y \in [-L_y/2, L_y/2], \\ G_\alpha(x, -L_y/2) = G_\alpha(x, L_y/2), \quad \forall x \in [-L_x/2, L_x/2]. \end{cases} \tag{4.25}$$

To obtain G_α we use the method of the image and the fact that the Green's function solution in the free space of the Helmholtz operator L_α^{-1} is given by $-K_0\left(r/\alpha\right)/(2\pi\alpha)$, where K_0 is the modified Bessel function of the second kind of zeroth-order. Hence

$$G_\alpha = -\sum_{m,n\in\mathbb{Z}} \frac{1}{2\pi\alpha^2} K_0\left(\frac{\sqrt{(x-mL_x)^2+(y-nL_y)^2}}{\alpha}\right)$$

and

$$\begin{aligned} \Psi^{\alpha}_{L_x,L_y}(x,y) = \frac{x^2}{2L_xL_y} - \frac{1}{2\pi}\log\left|\theta_1\left(\pi(i\frac{x}{L_y}+\frac{y}{L_y}), e^{-\pi\frac{L_x}{L_y}}\right)\right| + \\ - \sum_{m,n\in\mathbb{Z}} \frac{1}{2\pi} K_0\left(\frac{\sqrt{(x-mL_x)^2+(y-nL_y)^2}}{\alpha}\right). \end{aligned} \tag{4.26}$$

The Euler-α regularization of the BR equation is given by

$$\frac{\partial \mathbf{x}_\alpha(p,t)}{\partial t} = \int_{-L_x/2}^{L_x/2} \gamma(\tilde{p}) \mathbf{K}^{\alpha}_{L_x,L_y}(\mathbf{x}(p,t) - \mathbf{x}(\tilde{p},t)))d\tilde{p}, \tag{4.27}$$

with $\mathbf{K}^{\alpha}_{L_x,L_y}$ obtained from (4.21) and (4.26).

Numerical solution of (4.27) is obtained by using the same procedures adopted for the non-regularized BR equation. To compute G_α, thanks to the rapid decay of K_0, it is enough, at least for the values of the parameter α we have chosen, to add only the terms with $m, n \leq 2$.

4.2 Roll-up phenomena in the regularized BR-α model

The BR-α model allows to continue the vortex-sheet motion after the singularity time t_s, see [41]. We have performed several numerical simulations of (4.27) with the initial condition (3.16) and with different values for the regularization parameter, $\alpha = 0.1, 0.05, 0.01$. Vortex sheet behavior at time $t = 1.505$, just prior the singularity time of the non-regularized BR solution, is shown in Fig.4a for the various α and compared with the BR solution: as expected, taking smaller α values, the BR-α solution shows a better agreement with the BR case. This results is confirmed in Fig.4b-c where the curvature κ and

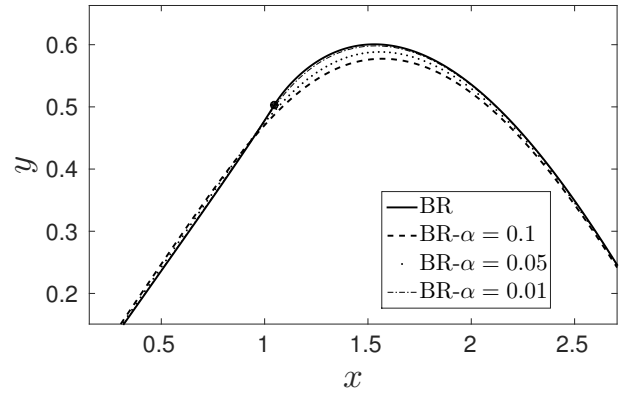

(a)

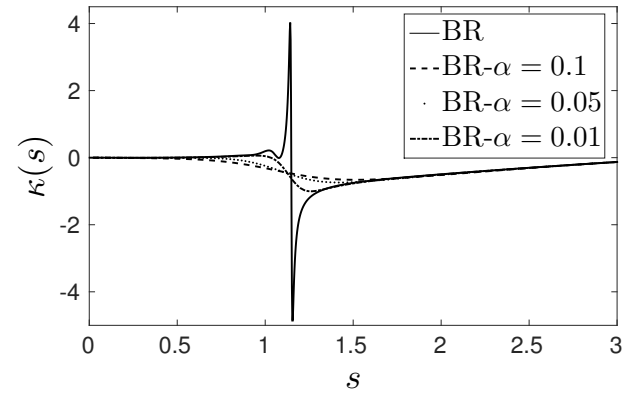

(b)

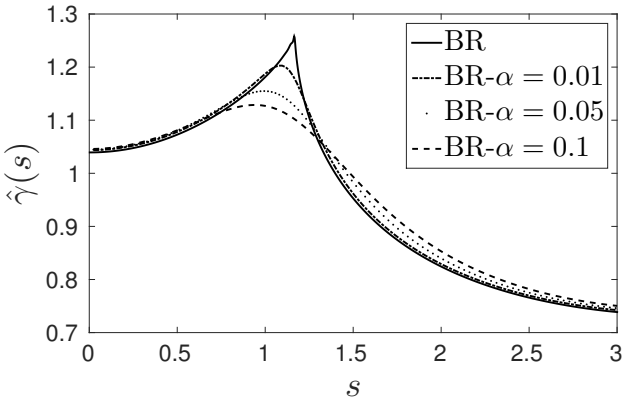

(c)

Fig. 4 a) Vortex sheet curve at $t = 1.505$ for BR solution and BR-α solution. The black dot is the point where singularity forms in the component of the BR solution at $t_s = 1.507$. The BR-α curve better approximates the BR curve by decreasing α.**b)** Signed curvature κ as function of the signed arc length $s(p)$ starting from $p = 0$. In the BR case, the curvature is strongly increasing positively at $s(p) \approx 1.16^-$ and negatively at $s(p) \approx 1.16^+$, and at t_s it diverges as an inverse of a square-root singularity. The BR-α curvature better approximates the BR curvature by decreasing α. **c)** True vortex-strength $\hat{\gamma}$ as function of the signed arc length $s(p)$. In the BR case $\hat{\gamma}$ has a cusp behavior at $s(p^*) \approx 1.16$, and at t_s develops a square-root singularity. The BR-α vortex-strength better approximates the BR vortex-strength by decreasing α.

the true vortex-strength $\hat{\gamma}$ are shown at the same time for the various α and compared with the BR case: the regularizing effects in the BR-α solution are here more evident and, while approaching as α decreases the configuration of the BR case, both κ and $\hat{\gamma}$ have smooth behavior.

After the singularity time t_s for the BR solution, the vortex-sheet motion given by the BR-α model is characterized by the typical roll-up phenomenon leading to spiral formation: this is clearly visible in Fig.5, Fig.7a and Fig.8a for the various α at different times. The precursor of the spiral formation is the first winding formation. It can be detected by the presence on the sheet of two consecutive particles moving in opposite directions, so that, at a specific time, they have the same tangential component; this is equivalent to the condition $\partial_p x(p,t) = 0$ which is verified at $t \approx 3.1, 2.46, 1.81$ for $\alpha = 0.1, 0.05, 0.01$, respectively, and at the spatial location having the highest true vortex-strength, i.e. the core of the sheet. After the formation of this first winding, the roll-up phenomenon is significantly faster for smaller values of α.

To better understand how the sheets evolves, we now give a detailed explanation of the roll-up evolution for the case $\alpha = 0.01$. In Figs.6a-f the curvature κ and the true vortex strength $\hat{\gamma}$ are shown at different times. At $t = 1.89$ the first winding has done a complete turn around the core of the vortex sheet; at this time a significant quantity of vorticity has accumulated close to the core of the sheet placed in $s \approx 1.146$ where $\hat{\gamma}$ has its maximum value which is now 7.25, about six times the maximum value of $\hat{\gamma}$ at $t = 1.505$, compare to Fig.4c. The increasing value of $\hat{\gamma}$ in the core physically expresses a compression of particles close to the core. Particle compression in the core also leads to the stretching of the arms of the spiral, as particles on the arms of sheets tend to depart from each other, leading to the growth of $\partial_p s$ in the points of maximum stretching and the consequent minima formation in $\hat{\gamma}$ visible in figure in $s \approx 1.07, 1.23$. In the core of the sheet, to be more precise in $s \approx 1.144$ (positive curvature) and in $s \approx 1.147$ (negative curvature), κ has dramatically increased its values which is now about 140 times larger than the curvatures at $t = 1.505$, see Fig.4b. The increasing curvature close to the core of the sheet is the typical effect characterizing the curvature singularity seen in the non regularized BR equation, see Figs.4b-c. However the regularized BR-α evolution of the sheet leads to the formation of other points of local increasing curvature in $s \approx 1.117$ (positive) and in $s \approx 1.179$ (negative). At the same time also a secondary local maximum in $\hat{\gamma}$ is already formed in $s \approx 1.17$ and another one is just formed at $s \approx 1.179$, meaning that particles are locally compressed in these two points of the arms of the spiral, supporting the roll-up phenomenon with the formation of consequent high curvature points. The vortex-strength of the two local maxima is significantly weaker than the vortex-strength of the core, being $\hat{\gamma}(1.17) \approx 0.85$ and $\hat{\gamma}(1.179) \approx 0.79$.

As time passes the strength of the core becomes stronger, being $\hat{\gamma} \approx 10.22$. At this time the curve is stretched in two other points close to the core and leading, as before, to the formation of two other local maxima in $\hat{\gamma}$, as visible in Fig.6c at $t = 1.95$: the points are located in $s \approx 1.189$ and $s \approx 1.26$, between the core and the two previous local maxima formed at $t = 1.89$.

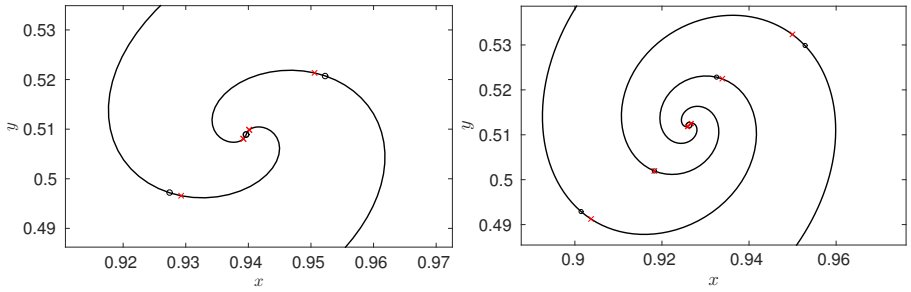

(a) $\alpha = 0.01, t = 1.89$ (b) $\alpha = 0.01, t = 1.95$

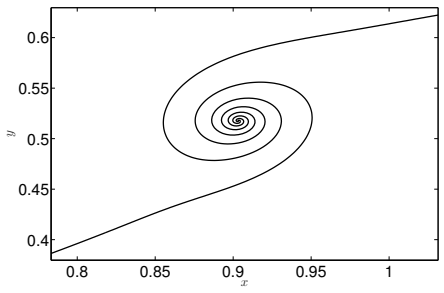

(c) $\alpha = 0.01, t = 2.05$

Fig. 5 Vortex-sheet motion for $\alpha = 0.01$ at several times. In (a)-(b) the black circles are points in which the true vortex-strength has its maxima, while the crosses are the points in which the curvature increases its amplitude (see also Fig.6) .

These two high-strength points however are weaker than the previous pair as $\hat{\gamma}(1.189) \approx 0.57$ and $\hat{\gamma}(1.26) \approx 0.52$; likewise, the pair of the previous local maxima, now located in $s \approx 1.2$ and $s \approx 1.328$, weaken, being their vortex-strength halved with respect the time $t = 1.89$. At the same time two points of increasing curvature are formed in $s \approx 1.186$ (positive) and $s \approx 1.264$ (negative). As time passes the formation of local maxima in $\hat{\gamma}$ and the local maxima/minima in κ is more evident, as shown at $t = 2.05$ in Figs.6e-f. As we shall see in the next subsection, these critical points are all related to the presence of complex singularities different from the BR complex singularity responsible for the curvature divergence in the non-regularized case.

For larger values of α the spiral formation is slower, and the first winding in the roll up process begins later. When $\alpha = 0.1$ the appearance of solution at time $t = 4.9$ is similar to the solution for $\alpha = 0.01$ at time $t = 1.95$; an analogous similarity is observed with the solution for $\alpha = 0.05$ at time 3.35. At these times, in fact, for both $\alpha = 0.1, 0.05$ there are four arms formed in the spiral as in the case $\alpha = 0.01$, as shown in Figs.7a-8a. Moreover, as for $\alpha = 0.01$, there are two pairs of local maxima in $\hat{\gamma}$ on the left and on the right of the core (see Figs.7b-8b), and two pairs of local maxima/minima in κ on the left and on the right of the core, see Figs.7c-8c. The main differences

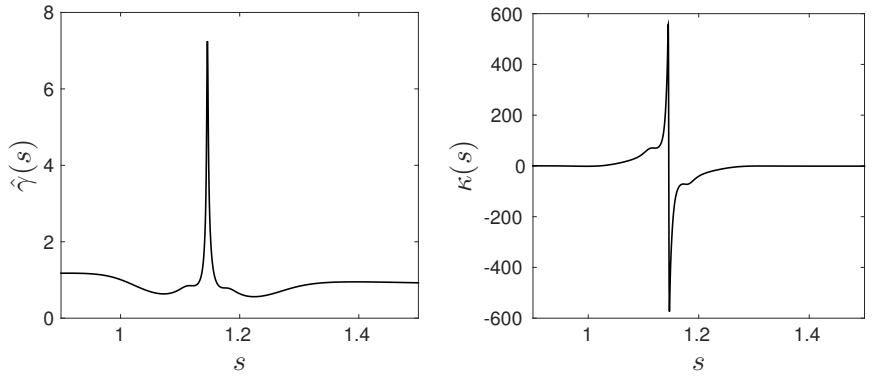

(a) $\alpha = 0.01, t = 1.89$

(b) $\alpha = 0.01, t = 1.89$

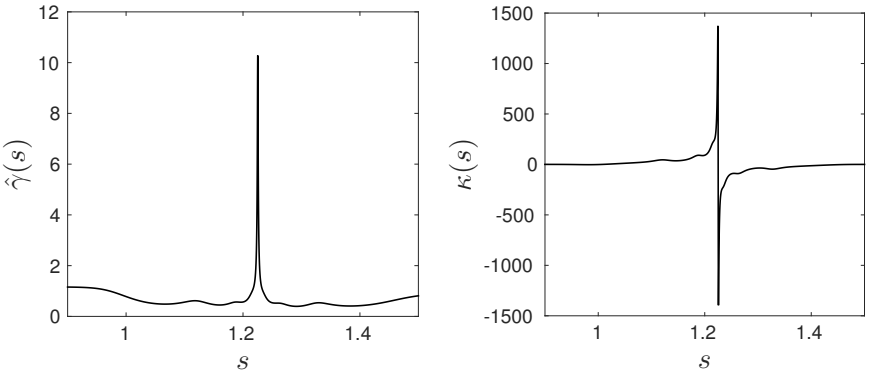

(c) $\alpha = 0.01, t = 1.95$

(d) $\alpha = 0.01, t = 1.95$

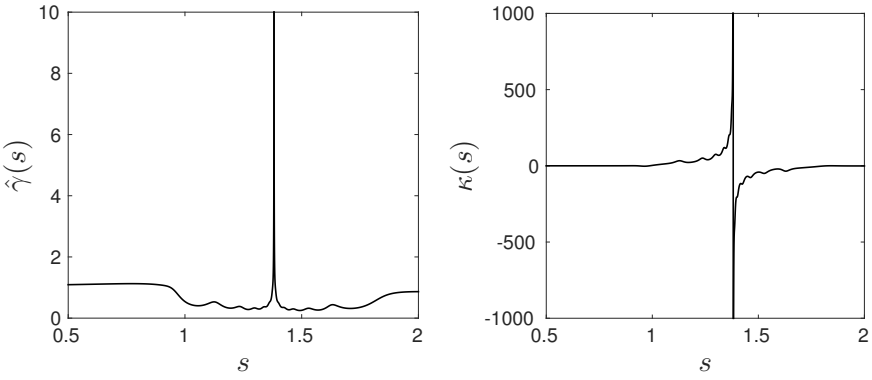

(e) $\alpha = 0.01, t = 2.05$

(f) $\alpha = 0.01, t = 2.05$

Fig. 6 Time evolution for the true vortex-strength $\hat{\gamma}$ and the curvature κ for $\alpha = 0.01$ at $t = 1.89, 1.95, 2.05$. In (c)-(f) figures are cut in their normal extension to better visualize the secondary maxima/minima points: the maximum of $\hat{\gamma}$ at $s = 1.381$ is 16, whereas the maximum/minimum of κ reaches 3500. As time passes, during the roll up process, several local maxima/minima form in both $\hat{\gamma}$ and κ.

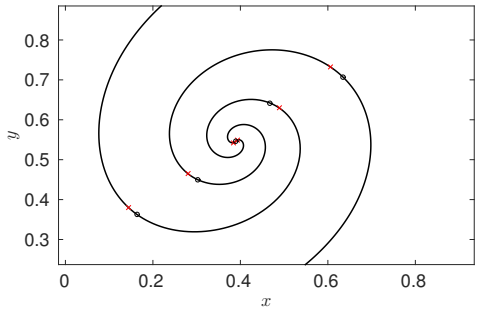

(a) $\alpha = 0.1, t = 4.9$

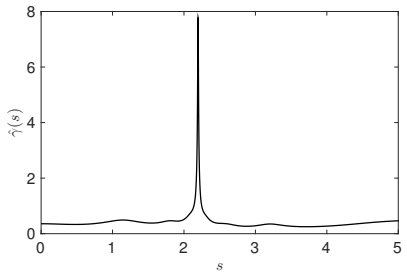

(b) $\alpha = 0.1, t = 4.9$

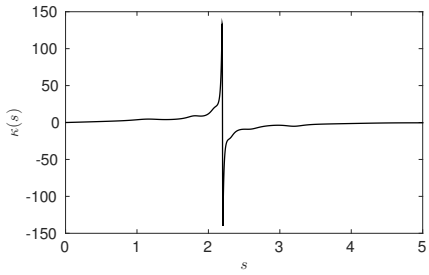

(c) $\alpha = 0.1, t = 4.9$

Fig. 7 (a) Vortex sheet curve for $\alpha = 0.1$ at $t = 4.9$. Black circle are point of maximum vortex strength $\hat{\gamma}$, red corsses are points of local increasing curvature. **(b)** The true vortex-strength $\hat{\gamma}$ as a function of the signed arc length for $\alpha = 0.1$ at $t = 4.9$. **(c)** The curvature κ as function of the arc length for $\alpha = 0.1$ at $t = 4.9$.

between the various α can be summarized as follows: (i) the extension of the spiral diminishes as α decreases; (ii) the values of the maxima of $\hat{\gamma}$ and of the maxima/minima of κ increases as α decreases; (iii) the times when the various arms form are delayed for larger α.

4.3 Singularity Tracking for the BR-α model: comparison with the BR results

The aim of this subsection is to compare the complex singularities of the BR-α case with the analysis presented in Section 3.1 for the BR equation. Therefore we apply the singularity tracking methods to detect the complex singularities of the BR-α solution. In particular we use the Borel-Polya-van der Hoeven method (BPH) that was originally proposed in [58], and the Padé approximants, see the Appendix for more details.

Singularity tracking is applied to the Fourier expansion of the components $(X_\alpha(p,t), Y_\alpha(p,t)) = (x_\alpha(p,t) - p, y_\alpha(p,t))$ obtained from the numerical solution of (4.27). The crucial difference with respect to the BR case is that the α model shows the emergence of several complex singularities. Up to

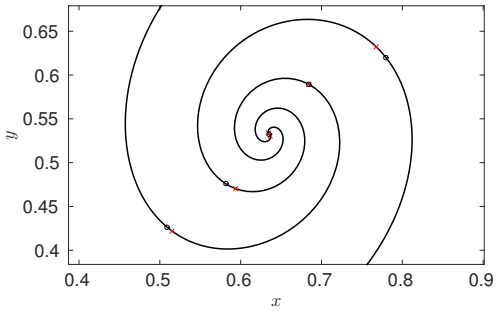

(a) $\alpha = 0.05, t = 3.35$

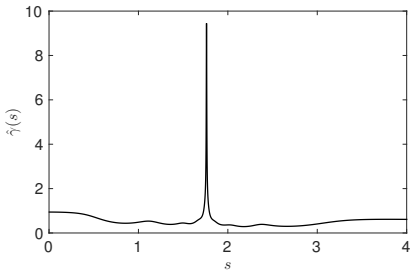

(b) $\alpha = 0.05, t = 3.35$

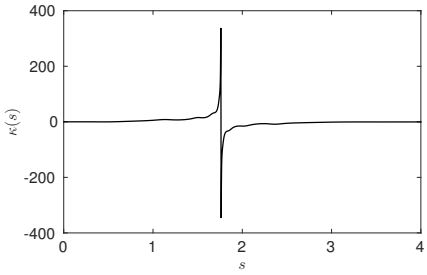

(c) $\alpha = 0.05, t = 3.35$

Fig. 8 **(a)** Vortex sheet curve for $\alpha = 0.05$ at $t = 3.35$. Black circle are point of maximum vortex strength $\hat{\gamma}$, red corsses are points of local increasing curvature. **(b)** The true vortex-strength $\hat{\gamma}$ as a function of the signed arc length for $\alpha = 0.05$ at $t = 3.35$. **(c)** The curvature κ as function of the arc length for $\alpha = 0.05$ at $t = 3.35$.

t_s we have clearly distinguished and characterized, in both the components X_α, Y_α, two main complex singularities whose location will be denoted with $\tilde{p}_1^\alpha = p_{1,\alpha} + i\delta_{1,\alpha}$ and $\tilde{p}_2^\alpha = p_{2,\alpha} + i\delta_{2,\alpha}$. Hereafter we shall also label these singularities simply with their locations $\tilde{p}_1^\alpha$ and $\tilde{p}_2^\alpha$. These singularities are tracked in time in the complexified p-plane from $t = 0.9$ up to $t = t_s$ and their trajectories are shown in Fig.9 [2]. For higher α, $\tilde{p}_1^\alpha$ and $\tilde{p}_2^\alpha$ remain quite distant from the real axis: this is the consequence of the regularizing effect due to the smoothing kernel (4.21). The characterizations $\mu_X^{\tilde{p}_1^\alpha}, \mu_Y^{\tilde{p}_1^\alpha}$ and $\mu_X^{\tilde{p}_2^\alpha}, \mu_Y^{\tilde{p}_2^\alpha}$ of the singularities are reported at $t = 1.505$ in Table 1, and they reveal that both components have a blow up in their second derivatives, compatible with the predicted values obtained from the singularity analysis in BR case.

[2] For $\alpha = 0.01$ the singularity $\tilde{p}_1^\alpha$ is clearly detected only from $t = 1.3$.

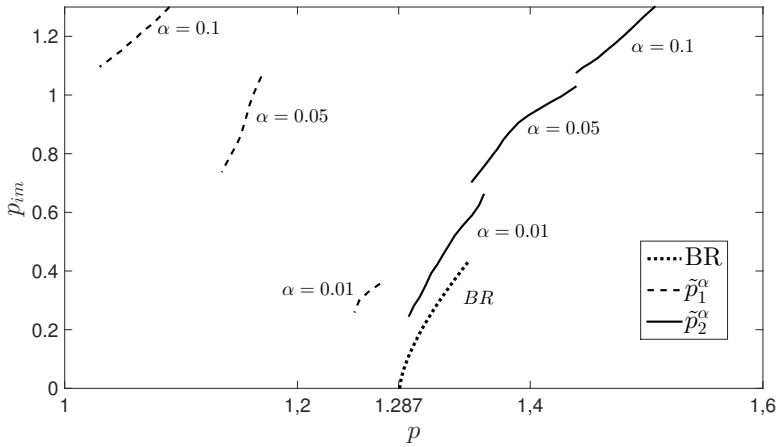

Fig. 9 The tracking of the complex singularities $\tilde{p}_1^\alpha$ and $\tilde{p}_2^\alpha$ of the components X_α of the BR-α solution from $t = 0.9$ up $t = t_s$ in the complex plane (p, p_{im}). For $\alpha = 0.01$, $\tilde{p}_1^\alpha$ is well detected only from $t = 1.3$. The dotted line is the tracking of the complex singularity of the BR solution. The singularity $\tilde{p}_2^\alpha$ is closer to the BR singularity and it is in general more closer to the real domain than $\tilde{p}_1^\alpha$. At $t = t_s$ the singularities have characterizations compatible with the predicted singularity characterization of the BR solution (see Table 1).

α	$\mu_X^{\tilde{p}_1^\alpha}$	$\mu_Y^{\tilde{p}_1^\alpha}$	$\mu_X^{\tilde{p}_2^\alpha}$	$\mu_Y^{\tilde{p}_2^\alpha}$	μ_κ^α
0.1	1.89	1.95	1.76	1.86	-0.22
0.05	1.85	1.94	1.74	1.81	-0.38
0.01	1.76	1.85	1.65	1.69	-0.41
0	1.61		1.72		-0.44

Table 1 The characterizations of the complex singularities $\tilde{p}_1^\alpha, \tilde{p}_2^\alpha$ of the components of the vortex-sheet curve and characterizations μ_κ^α of the main complex singularities of the curvature, (the case $\alpha = 0$ refers to the only singularity of the BR solution). Characterizations are evaluated at time $t = 1.505$.

4.4 Singularity Tracking for the BR-α model: curvature singularity effects in the roll-up process

Just before the BR singularity time, at $t = 1.505$, the curvature κ is very large also for the regularized version. This can be seen in Fig.4b where one observes two spikes localized close to the core of the sheet. Passing the BR singularity time, the roll-up process intensifies and the curvature spikes grow considerably, see Figs.6b. However we have observed that other points of locally increasing (positive and negative) curvature form along the various arms of the spiral. In this section we show that these new spikes are due to the presence of complex singularities in the curvature itself.

As done in Section 4.2 we describe the case $\alpha = 0.01$. The positions of the complex singularities of κ are obtained through the Padé approximants, and they are shown in Figs.10-12 at $t = 1.505, 1.89, 1.95$.

At $t = 1.505$ we have clearly detected one complex singularity placed in $\approx (1.205, 0.224)$. The singularity closest to the real domain corresponds to the point where the curvature has a sharp variation and obviously coincides with the maximum of the true vortex strength. This agrees with the results we obtained in the BR case, where the singularity in the curvature causes, just before the singularity formation, a rapid variation from a diverging positive curvature to a diverging negative one, see Fig.4b. By applying the BHP method we have obtained that this singularity has characterization $\mu_\kappa^\alpha = -0.41$, in very good agreement with the value -0.46 predicted in the BR case (the characterizations for $\alpha = 0.1, 0.05$ are shown in Table1, and they also agree with the values -0.46). One can therefore conclude that this complex singularity is the regularized counterpart of the real BR curvature singularity.

In the same figure appear two additional complex singularities; with respect to the main singularity, they are placed on the left and on the right. At the time shown the presence of these singularities has no physical counterpart; however these two secondary singularities anticipate the formation of the points of locally increasing curvature that we have previously examined in Section 4.2, see Fig.5b and Fig.11. In fact, at $t = 1.89$, the singularities previously detected at $t = 1.505$ are now closer to the real axis, and the real part of their complex position strictly corresponds to the arc length values where the curvature increases, see Fig.6b. Moreover, several other singularities are visible and approaching the real axis. At $t = 1.95$, the singularities are still closer to the real axis, and other singularities are clearly detected by the Padé approximants.

5 The Euler evolution of a vortex layer

In this Section we perform a comparison of the results obtained for the BR-α model with the motion of a vortex layer of small thickness. This problem has been addressed by several authors. Moore and Dhanak in [54] and [28], through a matched asymptotic expansion, derived a correction to the BR equation that takes into account the effect of the thickness of the layer. A recent investigation [64] seems to show that these corrections are not able to prevent singularity formation. In [6] the authors performed an extensive numerical investigation considering the case of a layer of uniform thickness: their analysis is based on a system governing the two interfaces bounding the vorticity layer. Benedetto and Pulvirenti, in the paper [12] concerning the rigorous analysis of the dynamics of a layer of uniform vorticity, proved the convergence, for a short time, toward the BR dynamics.

We consider an incompressible 2D inviscid flow with initial vorticity concentrated on a layer of small thickness ϵ while, outside the layer, vorticity rapidly decays. If one introduces the rescaled variable $Y = (y - \phi(x))/\varepsilon$, we assume the initial vorticity to be of the form

$$\omega_0(x, y) = \varepsilon^{-1} f(x, Y) \tag{5.28}$$

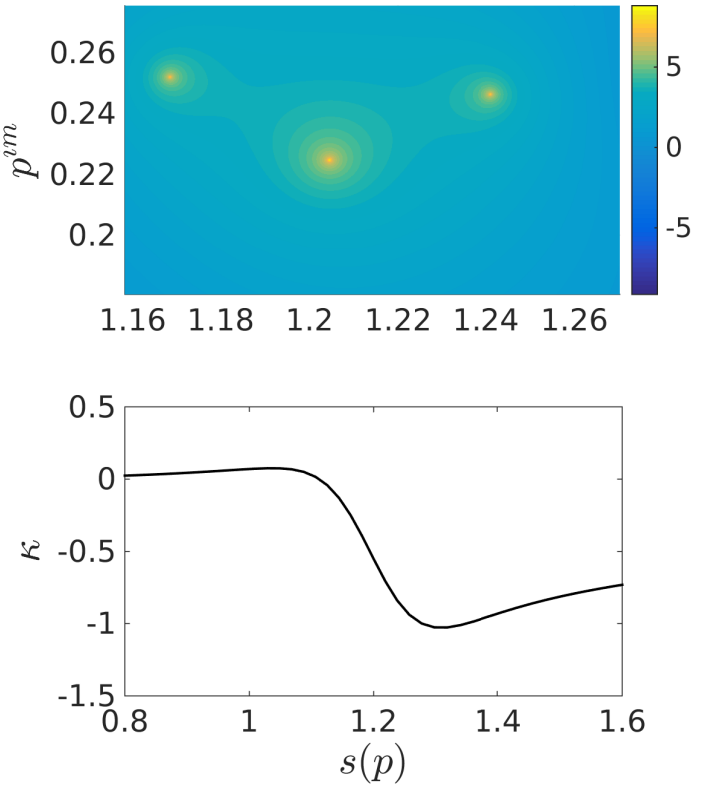

Fig. 10 In the upper figure the log-modulus in the complex plane $(s(p), p^{im})$ of the Padé approximants $P_{100/100}$ of the curvature (shown in the lower figure) for $\alpha = 0.01$ at $t = 1.505$. Light/Yellow colors are relative to large values of the approximants. Singularities are placed where the approximants have large values. The singularity closest to the real domain is placed in (1.205,0.224) and it has a characterization of -0.41, in agreement with that predicted by the BR case. Two other complex singularities are also placed in on the left and on the right of the main one. These two secondary singularities correspond to points of increasing curvature that forms later in the curvature (see Fig.11)

where $f(x, Y)$ has a rapid, for example exponential, decay in Y, and $\int f(x, Y)dY$ is finite. Clearly the curve $y = \phi(x)$ represents the *center* of the layer and, in the limit of the thickness going to zero i.e. $\epsilon \to 0$, the layer shrinks to a sheet.

The governing equations for the flow evolution are the Euler equations that we shall solve using the vorticity-streamfunction formulation. The initial

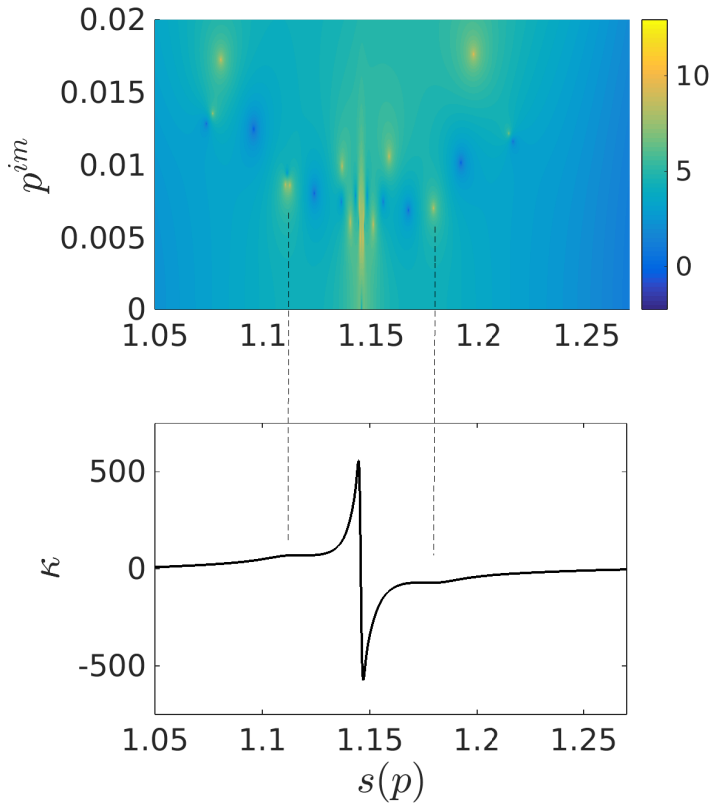

Fig. 11 In the upper figure the log-modulus in the complex plane $(s(p), p^{im})$ of the Padé approximants $P_{500/500}$ of the curvature (shown in the lower figure) for $\alpha = 0.01$ at $t = 1.89$. Light/Yellow colors are relative to high values of the approximants. Singularities are placed where the approximants have large values. The singularities are closer to the real axis with respect the time $t = 1.505$. At this time, these singularities strictly correspond to points of increasing curvature. Dashed lines mark the correspondences between the singularities and the secondary maxima/minima already formed in the curvature.

datum we shall consider is of a vortex layer type:

$$\partial_t \omega + u\partial_x \omega + v\partial_y \omega = 0 \tag{5.29}$$
$$\partial^2_{xx}\psi + \partial^2_{yy}\psi = -\omega, \tag{5.30}$$
$$u = \partial_y \psi, \quad v = -\partial_x \psi, \tag{5.31}$$
$$\omega(x, y, t = 0) = \omega_0(x, y), \tag{5.32}$$
$$\phi(x) = \sin(x)/2, \tag{5.33}$$
$$f(x, Y) = \exp\left(-Y^2/2\right)/\sqrt{2\pi}. \tag{5.34}$$

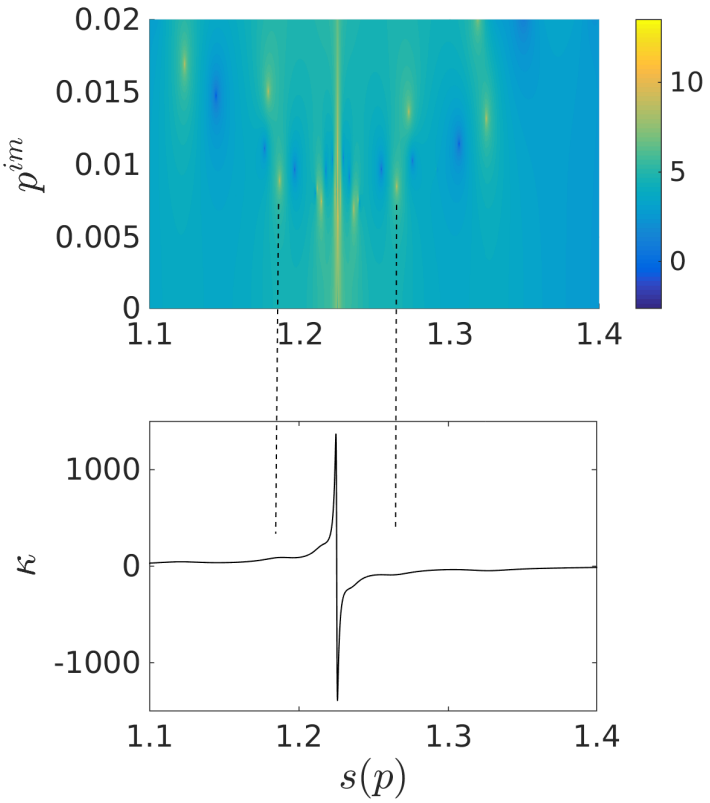

Fig. 12 Same as Figs.10-11 for $\alpha = 0.01$ at $t = 1.95$.

Equation (5.29) is the vorticity-transport equation, (5.30) is the Poisson equation for the streamfunction, and equations (5.31) relate the velocity components to the streamfunction. The initial condition is given by (5.32), (5.33) and (5.34), being ω_0 defined in (5.28), and it expresses a positive vorticity highly concentrated on a small sinusoidal layer having thickness of order ϵ along the y-direction. The vorticity, in the layer, is distributed according to a gaussian centered on the curve $\phi(x)$.

It is useful to recover the time evolution of the material curve $\mathcal{C}$ which initially coincides with $(x, \phi(x))$. In fact, in the limit of zero thickness, the $\mathcal{C}$ is exactly the vortex sheet curve (3.16) used as initial configuration for the BR equation. One expects that the time evolution of the curve $\mathcal{C}$ should be predicted by the BR equation at least before the occurrence of the singularity, i.e. for $t < t_s$. Moreover the regularizing effect of the finite thickness of the layer prevents the singularity formation in the Euler solution, and it is of interest to analyze the time evolution of the layer for $t > t_s$.

The curve $\mathcal{C}$ is numerically approximated by placing, at $t = 0$, $N + 1$ fluid particles that are transported by the velocity field (u, v) obtained from the Euler solutions. Namely, let $(x_j(0), y_j(0))$ for $j = 0, \cdots N$, the particles initially placed at $(j\pi/N, \phi(j\pi/N)), \quad j = 0, \cdots N$. The Lagrangian evolution of the generic particle $(x_j(t), y_j(t))$ is governed by

$$\frac{dx_j}{dt} = u(x_j(t), y_j(t)), \tag{5.35}$$

$$\frac{dy_j}{dt} = v(x_j(t), y_j(t)), \tag{5.36}$$

being (u, v) the velocity field obtained from the Euler solution.

The problem is solved by imposing periodic boundary conditions for both the tangential and normal variable, and a fully spectral numerical scheme is used with a semi-implicit third order Runge-Kutta scheme as temporal discretization, see [70] for more details. At each time step, to solve Eqs.(5.35)–(5.36), the velocity field (u, v) is spectrally interpolated in the position of the particles $(x_j(t), y_j(t))$.

5.1 Roll-up process for the vortex layer

The vorticity and the corresponding material curve $\mathcal{C}$ are shown in Figs.13-14 for $\varepsilon^2 = 10^{-2}, 10^{-3}$. In all cases the vorticity is advected toward the core of the layer, with the consequent formation of a bulge in which the vorticity is mostly concentrated. As time passes the typical roll-up into a spiral precess is visible, with the formation of trailing arms that wrap around the core of the layer. However, the different initial thickness of the layer leads to a different flow motion. In fact for $\varepsilon^2 = 0.01$ the two symmetric cores tend to collide forming one big vorticity core; before this event, the material curve $\mathcal{C}$ has done only one complete turn around the center of the core. For $\varepsilon^2 = 0.001$, before the two core eventually collapse, several trailing arms form. This is visible at times $t = 4.0$ and $t = 5.0$, where we can also observe that the curve $\mathcal{C}$ has done three and four complete turns around the center of the core, respectively.

We can also notice that for $\varepsilon^2 = 0.01$, at $t = 5.0$, the shape of $\mathcal{C}$ resembles quite well the shape of the vortex sheet curve for $\alpha = 0.1$ at $t = 4.9$ in Fig.7a. Moreover the center of the core of the vortex-sheet for the BR-α (the point with highest true vortex strength) is placed in (0.38,0.54), while the center of the core of the vortex layer (the point with highest vorticity is placed in(0.35,0.55). Hence, although the BR$-\alpha$ and the layer of small thickness are different regularization of the BR model, it seems that they have a similar evolution after the singularity time t_s for the BR solution. This result is reminiscent of the investigation presented in [67] where the authors compared the motion a viscous layer of small thickness governed by the Navier-Stokes equation with the motion predicted by the vortex blob regularization of the BR equation (BR-δ regularization). By varying independently the viscosity ν

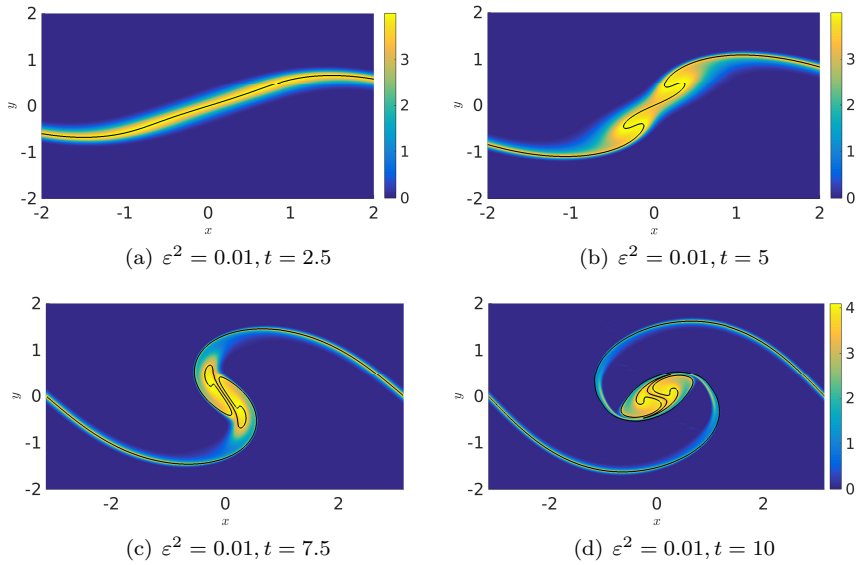

(a) $\varepsilon^2 = 0.01, t = 2.5$ (b) $\varepsilon^2 = 0.01, t = 5$

(c) $\varepsilon^2 = 0.01, t = 7.5$ (d) $\varepsilon^2 = 0.01, t = 10$

Fig. 13 The vorticity distribution at various time for $\varepsilon^2 = 0.01$. The black lines represent the material curve $\mathcal{C}$ computed by (5.35)-(5.36). The roll up behavior predicted by the vortex sheet motion is visible. The pair of vorticity cores that form during the roll-up process eventually collapse on each other, forming a big core well visible at time $t = 10$.

of the flow and the thickness ϵ of the layer, in [67], it is shown that, in the limit $\nu \to 0$ and $\epsilon \to 0$, the time evolution of the material curve obtained from Navier-Stokes calculation well approximates the vortex-sheet computed with the BR-δ regularization.

6 Conclusions

We have analyzed the roll-up phenomenon for the BR-α equation in terms of the complex singularities for an infinite array of vortex sheets. The non-regularized BR equation ($\alpha = 0$) develops a $3/2$ branch singularity in the components of the curve and a $-1/2$ singularity in the curvature. After the singularity time the BR-α solution is characterized by the roll-up phenomenon with spiral formation. A key result we have obtained is the detection, in the BR-α solution, of several complex singularities. We have related these singularities to the points having the highest curvature along the arms of the spiral. The singularities of the regularized solution have the same characterization of the BR singularity, that is $3/2$ branch singularity for the curve components, and $-1/2$ singularity for the curvature.

We have also seen how the BR-α model gives an excellent approximation of the motion of a vortex layer or, to be more precise, of the lagrangian motion of the center of the layer. The vorticity concentration we have observed might

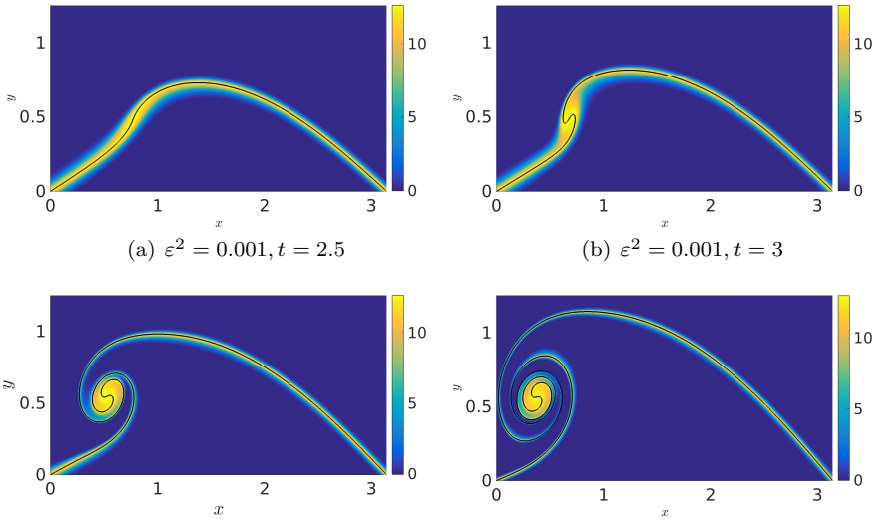

(a) $\varepsilon^2 = 0.001, t = 2.5$ (b) $\varepsilon^2 = 0.001, t = 3$

(c) $\varepsilon^2 = 0.001, t = 4$ (d) $\varepsilon^2 = 0.001, t = 5$

Fig. 14 The vorticity distribution at various time for $\varepsilon^2 = 0.001$. The black lines represent the material curve $\mathcal{C}$ computed by (5.35)-(5.36). With respect to the case $\varepsilon^2 = 0.01$ the roll up behavior leads to a spiral having several arms. At $t = 5$ one big core of vorticity (and its symmetry in the third quadrant) is formed with two thin braids of vorticity around it.

suggest a relationship with the Di Perna and Majda theory [29,30], as pointed out in [6]. Notice also how, when $\alpha \to 0$, all the detected complex singularities seem to coalesce.

There are many possible regularization procedure that allows the continuation of the vortex-sheet motion beyond the singularity time: the vortex blob methods, as numerical tool, has been employed since the first stages of the investigation on vortex-sheets, see e.g. [46,45,18]; the approximation with viscous layers has a fundamental importance because it is what one might think to be the best approximation of the physical reality. It would be interesting to see whether these regularized models show the appearance of complex singularities as for the BR-α model and, in case, compare the singularity behavior deriving from the different regularizations. This topic is under current investigation [16] and will appear elsewhere.

A Singularity tracking methods

The singularity tracking method based on the asymptotic ansatz (3.17) has the advantage to be of easy implementation, but it has the relevant drawback that it gives information only on the complex singularity closest to the real axis. To retrieve information on the possible other singularities outside the width of the analyticity strip, one can use two other methods which, as we shall explain in this appendix, should be used together to obtain more robust results.

The first method used is the so called BPH (Borel-Polya-Van der Hoeven) method, originally proposed in [58] to characterize all the complex singularities for the Burgers equation. It is based on an asymptotic ansatz given by Polya ([60]) for a Borel series obtained from a Taylor series. In particular, given the inverse Taylor series $f(z) = \sum_{k=0}^{N} f_k/z^{k+1}$ that has n complex singularities $c_j = |c_j|\mathrm{e}^{-i\rho_j}$ for $j = 1, 2, \ldots, n$, its Borel transform is given by $U_B(\zeta) = \sum_{k=0}^{N} f_k\zeta^k/k!$. Evaluating the modulus of the Borel series $G(r) = |U_B(r\mathrm{e}^{i\phi})|$ along the rays $r\mathrm{e}^{i\phi}$, one obtains, through a steepest descent argument, the following asymptotic behaviour

$$G(r) \approx C(\phi)r^{-(\mu(\phi)+1)}\mathrm{e}^{h(\phi)r} \quad \text{for} \quad r \to \infty. \tag{A.37}$$

The *indicatrix* function $h(\phi)$ is the piecewise cosine function

$$h(\phi) = |c_j|\cos(\phi - \rho_j) \quad \text{for} \quad \phi_{j-1} < \phi < \phi_j, \tag{A.38}$$

where the angular intervals (ϕ_{j-1}, ϕ_j) depend on the complex positions of the singularities (we refer to [58] for a deeper explanation on how the set ϕ_j, $j = 1, 2, \ldots, n$ is determined). Therefore, through numerical interpolation we can determine the parameters $|c_j|$ and ρ_j that give the locations of the complex singularities c_j. In practice, for each direction ϕ we need to determine the exponential rate of (A.37) that allows for construction of the indicatrix function h. Moreover, an estimate of $\mu(\rho_j)$ in (A.37) returns the characterization of the singularity c_j. The BPH method can be easily applied to Fourier series $u(z) = \sum_{k=-K/2}^{k=K/2} u_k\mathrm{e}^{ikz}$ by writing u as a Taylor series. This is accomplished by introducing the complex variables $Z_+ = e^{iz}, Z_- = e^{-iz}$ so that

$$u(z) = \sum_{k=0}^{K/2} u_k e^{ikz} + \sum_{k=1}^{K/2} u_k e^{-ikz} = \sum_{k=0}^{K/2} u_k/Z_+^k + \sum_{k=1}^{K/2} u_k/Z_-^k \tag{A.39}$$

The advantage of this methodology with respect to the singularity tracking method lies in the fact that it is possible to capture information on all the singularities located in the convex hull outside the radius of convergence of a Taylor series (or the strip of analyticity of a Fourier series). However some drawbacks are present. In fact singularities close to each other could be difficult to distinguish, and the various cosine function in (A.38) can be numerically determined along different range of r.

As already done in [37] to detect the complex singularities of the wall shear of Navier-Stokes equation, it is strongly suggested to obtain preliminary information on the position of the complex singularities, so that one can search for the specific cosine functions forming the indicatrix function. This is accomplished with the second method we have used, the Padé approximation . We recall that the Padé approximant

$$P_{L/M} = \frac{\sum_{i=0}^{L} a_i z^i}{1 + \sum_{j=1}^{M} b_j z^j} \tag{A.40}$$

is a rational function which approximates a complex function $f(z)$ as

$$f(z) - P_{L/M}(z) = O(z^{L+M+1}). \tag{A.41}$$

If $f(z) = \sum_{k=0}^{\infty} f_i z^k$, the M unknown denominator coefficients $b_j, j = 1 \ldots, M$ and the $L + 1$ unknown numerator coefficients $a_i, i = 0, \ldots, L$ are determined uniquely by (A.41). This means that the following set of linear equations must be solved

$$\sum_{i=0}^{\min(\alpha,M)} b_i c_{\alpha-i} = a_\alpha \quad \alpha = 0, \ldots, L; \qquad \sum_{i=0}^{M} b_i c_{L+\beta-i} = 0, \quad \beta = 1, \ldots, M.$$

Padé approximants are easy compute for Fourier series: given $u(x) = \sum_{k=-K}^{K} \hat{u}_k e^{ikx}$, then its Padé approximants can be derived considering the Fourier series as the sum of two power series in the complex variables $z_+ = e^{ix}$ and $z_- = e^{-ix}$, i.e.

$$u(z) \approx P_{L/M}(z_+) + Q_{L/M}(z_-) - \hat{u}_0, \tag{A.42}$$

with $L+M+1 = N$, and $P_{L/M}(z_+)$ and $Q_{L/M}(z_-)$ are respectively the Padé approximants of $\sum_{k=0}^{N} \hat{u}_k z_+^k$ and $\sum_{k=0}^{N} \hat{u}_k z_-^k$, see [7,68]. The main drawbacks of the Padé approximation is that it gives no information about the characterizations of the singularities. Moreover it is unable to distinguish between poles and branch singularities, as branch cut are approximated by a sequence of poles where the cut should be. However, for our purpose, we need only to detect the position of the singularities, and this can be done by simply extrapolate the zeros of the denominator in (A.40).

Acknowledgements The work of FG and VS has been partially supported by the *Progetti Giovani GNFM 2015* grant.

References

1. D.H. Bailey, J.M. Borwein, R.E. Crandall, and I.J. Zucker, *Lattice sums arising from the Poisson equation*, J. Phys. A: Math. Theor. **46** (2013), no. 11, 115201.
2. G. R. Baker and J.T. Beale, *Vortex blob methods applied to interfacial motion*, J. Comp. Phys. **196** (2004), no. 1, 233 – 258.
3. G. R. Baker, R.E. Caflisch, and M. Siegel, *Singularity formation during Rayleigh-Taylor instability*, J. Fluid Mech. **252** (1993), 51–75.
4. G. R. Baker, D. I. Meiron, and S. A. Orszag, *Generalized vortex methods for free-surface flow problems*, J. Fluid Mech. **123** (1982), 477–501.
5. G. R. Baker and L. D. Pham, *A comparison of blob methods for vortex sheet roll-up*, J. Fluid Mech. **547** (2006), 297–316.
6. G. R. Baker and M. J. Shelley, *On the connection between thin vortex layers and vortex sheets*, J. Fluid Mech. **215** (1990), 161–194.
7. G.A. Baker, Jr. and P. Graves-Morris, *Padé approximants*, second ed., Encyclopedia of Mathematics and its Applications, vol. 59, Cambridge University Press, Cambridge, 1996.
8. C. Bardos, J. S. Linshiz, and E. S. Titi, *Global regularity for a Birkhoff-Rott-α approximation of the dynamics of vortex sheets of the 2d Euler equations*, Physica D: Nonlinear Phenomena **237** (2008), no. 14-17, 1905–1911.
9. C. Bardos, J.S. Linshiz, and E. S. Titi, *Global regularity and convergence of a Birkhoff-Rott-α approximation of the dynamics of vortex sheets of the two-dimensional Euler equations*, Comm. Pure Appl. Math. **63** (2010), no. 6, 697–746.
10. D. Benedetto, E. Caglioti, and C. Marchioro, *On the motion of a vortex ring with a sharply concentrated vorticity*, Math. Methods Appl. Sci. **23** (2000), no. 2, 147–168.
11. D. Benedetto, C. Marchioro, and M. Pulvirenti, *The 2-D incompressible Euler flow for singular initial conditions*, Nonlinear variational problems and partial differential equations (Isola d'Elba, 1990), Pitman Res. Notes Math. Ser., vol. 320, Longman Sci. Tech., Harlow, 1995, pp. 57–74.
12. D. Benedetto and M. Pulvirenti, *From vortex layers to vortex sheets*, SIAM J. Appl. Math. **52** (1992), no. 4, 1041–1056.
13. Garrett Birkhoff and Joseph Fisher, *Do vortex sheets roll up?*, Rendiconti del Circolo Matematico di Palermo **8** (1959), no. 1, 77–90.
14. R.E. Caflisch, *Singularity formation for complex solutions of the 3D incompressible Euler equations*, Physica D **67** (1993), no. 1-3, 1–18.
15. R.E. Caflisch, F. Gargano, M. Sammartino, and V. Sciacca, *Complex singularities and PDEs*, Rivista di Matematica della Universita di Parma **6** (2015), no. 1, 69–133.
16. ———, *Complex singularity analysis of vortex layer flow*, (2016), in preparation.
17. R.E. Caflisch, M.C. Lombardo, and M. Sammartino, *Vortex layers of small thickness*, (2016), in preparation.
18. R.E. Caflisch and J.S. Lowengrub, *Convergence of the vortex method for vortex sheets*, SIAM J. Numer. Anal. **26** (1989), no. 5, 1060–1080. MR 1014874
19. R.E. Caflisch and O.F. Orellana, *Long time existence for a slightly perturbed vortex sheet*, Comm. Pure Appl. Math **39** (1986), 807–838.

20. ———, *Singular solutions and ill-posedness for the evolution of vortex sheets*, SIAM J. Math. Anal. **20** (1989), no. 2, 293–307.
21. G.F. Carrier, M. Krook, and C.E. Pearson, *Functions of a Complex Variable: Theory and Technique*, McGraw–Hill, New York, 1966.
22. M. J. Chen and L. K. Forbes, *Accurate methods for computing inviscid and viscous Kelvin-Helmholtz instability*, Journal of Computational Physics **230** (2011), no. 4, 1499 – 1515.
23. C. Cichowlas and M.-E. Brachet, *Evolution of complex singularities in Kida-Pelz and Taylor-Green inviscid flows*, Fluid Dyn. Res. **36** (2005), no. 4-6, 239–248.
24. G.M. Coclite, F. Gargano, and V. Sciacca, *Analytic solutions and singularity formation for the peakon b-family equations*, Acta Appl. Math. **122** (2012), 419–434.
25. S.J. Cowley, *Computer extension and analytic continuation of Blasius' expansion for impulsively flow past a circular cylinder*, J. Fluid Mech. **135** (1983), 389–405.
26. S.J. Cowley, G.R. Baker, and S. Tanveer, *On the formation of Moore curvature singularities in vortex sheets*, J. Fluid Mech. **378** (1999), 233–267.
27. G. Della Rocca, M.C. Lombardo, M. Sammartino, and V. Sciacca, *Singularity tracking for Camassa-Holm and Prandtl's equations*, Appl. Numer. Math. **56** (2006), no. 8, 1108–1122.
28. M.R. Dhanak, *Equation of motion of a diffusing vortex sheet*, J. Fluid Mech. **269** (1994), 265–281.
29. R.J. DiPerna and A.J. Majda, *Concentrations in regularizations for* 2*-D incompressible flow*, Comm. Pure Appl. Math. **40** (1987), no. 3, 301–345.
30. ———, *Oscillations and concentrations in weak solutions of the incompressible fluid equations*, Comm. Math. Phys. **108** (1987), no. 4, 667–689.
31. J. Duchon and R. Robert, *Global vortex sheet solutions of euler equations in the plane*, Journal of Differential Equations **73** (1988), no. 2, 215 – 224.
32. C. Foias, D.D. Holm, and E.S. Titi, *The Navier-Stokes-α model of fluid turbulence*, Phys D. **152-153** (2001), 505–519.
33. U. Frisch, T. Matsumoto, and J. Bec, *Singularities of Euler flow? Not out of the blue!*, J. Stat. Phys. **113** (2003), no. 5, 761–781.
34. F. Gargano, G. Ponetti, M. Sammartino, and V. Sciacca, *Complex singularities in KdV solutions*, Ricerche di Matematica (2016), doi: 10.1007/s11587-016-0269-9.
35. F. Gargano, M. Sammartino, and V. Sciacca, *Singularity formation for Prandtl's equations*, Physica D: Nonlinear Phenomena **238** (2009), no. 19, 1975–1991.
36. F. Gargano, M. Sammartino, and V. Sciacca, *High Reynolds number Navier-Stokes solutions and boundary layer separation induced by a rectilinear vortex*, Computers & Fluids **52** (2011), 73–91.
37. F. Gargano, M. Sammartino, V. Sciacca, and K. W. Cassel, *Analysis of complex singularities in high-Reynolds-number Navier-Stokes solutions*, J. Fluid Mech. **747** (2014), 381–421.
38. F. Gargano, M. Sammartino, V. Sciacca, and K.W. Cassel, *Viscous-inviscid interactions in a boundary-layer flow induced by a vortex array*, Acta Appl. Math. **132** (2014), 295–305.
39. D.D. Holm, J.E. Marsden, and T.S. Ratiu, *The euler–Poincaré equations and semidirect products with applications to continuum theories*, Advances in Mathematics **137** (1998), no. 1, 1–81.
40. D.D. Holm, J.E. Marsden, and T.S. Ratiu, *Euler-Poincaré models of ideal fluids with nonlinear dispersion*, Phys. Rev. Lett. **80** (1998), no. 19, 4173–4176.
41. D.D. Holm, M. Nitsche, and V. Putkaradze, *Euler-alpha and vortex blob regularization of vortex filament and vortex sheet motion*, J. Fluid Mech. **555** (2006), 149–176.
42. C. Klein and K. Roidot, *Numerical study of shock formation in the dispersionless Kadomtsev-Petviashvili equation and dispersive regularizations*, Phys. D **265** (2013), 1–25.
43. ———, *Numerical study of the semiclassical limit of the Davey-Stewartson II equations*, Nonlinearity **27** (2014), no. 9, 2177–2214.
44. ———, *Numerical study of the long wavelength limit of the toda lattice*, Nonlinearity **28** (2015), no. 8, 2993–3025.
45. R. Krasny, *Desingularization of periodic vortex sheet roll-up*, Journal of Computational Physics **65** (1986), no. 2, 292 – 313.

46. ———, *A study of singularity formation in a vortex sheet by the point-vortex approximation*, J. Fluid Mech. **167** (1986), 65–93.
47. G. Lebeau, *Régularité du problème de Kelvin-Helmholtz pour l'équation d'Euler 2d*, ESAIM Control Optim. Calc. Var. **8** (2002), 801–825 (electronic), A tribute to J. L. Lions.
48. M.C. Lopes Filho, J. Lowengrub, H.J. Nussenzveig Lopes, and Y. Zheng, *Numerical evidence of nonuniqueness in the evolution of vortex sheets*, ESAIM: Math. Mod. and Num. Anal. **40** (2006), no. 2, 225–237.
49. C. Marchioro, *Euler evolution for singular initial data and vortex theory: a global solution*, Comm. Math. Phys. **116** (1988), no. 1, 45–55.
50. ———, *On the inviscid limit for a fluid with a concentrated vorticity*, Comm. Math. Phys. **196** (1998), no. 1, 53–65.
51. C. Marchioro and M. Pulvirenti, *Mathematical theory of incompressible nonviscous fluids*, Applied Mathematical Sciences, vol. 96, Springer-Verlag, New York, 1994.
52. T. Matsumoto, J. Bec, and U. Frisch, *The Analytic Structure of 2D Euler Flow at Short Times*, Fluid Dyn. Res. **36** (2005), no. 4-6, 221–237.
53. D.W. Moore, *The equation of motion of a vortex layer of small thickness*, Studies in Appl. Math. **58** (1978), no. 2, 119–140.
54. ———, *The spontaneous appearance of a singularity in the shape of an evolving vortex sheet*, Proc. Roy. Soc. London Ser. A **365** (1979), no. 1720, 105–119.
55. D.W. Moore, *Numerical and analytical aspects of Helmholtz instability*, Proceedings of the Sixteenth International Congress of Theoretical and Applied Mechanics, Lyngby, Denmark, 1985, pp. 263–274.
56. M. Nitsche, *Singularity formation in a cylindrical and a spherical vortex sheet*, J. Comp. Phys. **173** (2001), no. 1, 208 – 230.
57. M. Oliver and S. Shkoller, *The vortex blob method as a second-grade non-Newtonian fluid*, Comm. Partial Differential Equations **26** (2001), no. 1-2, 295–314. MR 1842434
58. W. Pauls and U. Frisch, *A Borel transform method for locating singularities of Taylor and Fourier series*, J. Stat. Phys. **127** (2007), no. 6, 1095–1119.
59. W. Pauls, T. Matsumoto, U. Frisch, and J. Bec, *Nature of Complex Singularities for the 2D Euler Equation*, Physica D **219** (2006), no. 1, 40–59.
60. G. Pólya, *Untersuchungen über Lücken und Singularitäten von Potenzreihen*, Math. Z. **29** (1929), 549–640.
61. K. Roidot and N. Mauser, *Numerical study of the transverse stability of NLS soliton solution in several classes of NLS-type equations*, arxiv:1401.5349 (2015).
62. P. G. Saffman, *Vortex dynamics*, Cambridge University Press, 1993.
63. M.J. Shelley, *A study of singularity formation in vortex–sheet motion by a spectrally accurate vortex method*, J. Fluid. Mech. **244** (1992), 493–526.
64. Sung-Ik Sohn, *Singularity formation and nonlinear evolution of a viscous vortex sheet model*, Physics of Fluids **25** (2013), no. 1, 014106.
65. C. Sulem, P.-L. Sulem, C. Bardos, and U. Frisch, *Finite time analyticity for the two- and three-dimensional Kelvin-Helmholtz instability*, Comm. Math. Phys. **80** (1981), no. 4, 485–516.
66. C. Sulem, P-L Sulem, and H. Frisch, *Tracing complex singularities with spectral methods*, J. Comput. Phys. **50** (1983), no. 1, 138–161.
67. G. Tryggvason, W.J.A Dahm, and K. Sbeih, *Fine structure of vortex sheet rollup by viscous and inviscid simulation*, Journal of Fluids Engineering **113** (1991), no. 1, 31–36.
68. J. A. C. Weideman, *Computing the dynamics of complex singularities of nonlinear PDEs*, SIAM J. Appl. Dyn. Syst. **2** (2003), no. 2, 171–186 (electronic).
69. Sijue Wu, *Mathematical analysis of vortex sheets*, Comm. Pure Appl. Math. **59** (2006), no. 8, 1065–1206.
70. X. Zhong, *Additive semi-implicit Runge–Kutta methods for computing high-speed nonequilibrium reactive flows*, J. Comp. Phys. **128** (1996), no. 1, 19–31.